Probing Electronic Coherence between Core-Level Vacancies at Different Atomic Sites

Jun Wang,[1,2,3,*] Taran Driver,[1,3,†] Paris L. Franz,[2,3] Přemysl Kolorenč,[4] Emily Thierstein,[1,2,3] River R. Robles,[2,3] Erik Isele,[1,2,3] Zhaoheng Guo,[2,3] David Cesar,[3] Oliver Alexander,[5] Sandra Beauvarlet,[1,11] Kurtis Borne,[3,10] Xinxin Cheng,[3] Louis F. DiMauro,[7] Joseph Duris,[3] James M. Glownia,[3] Martin Graßl,[1,3] Paul Hockett,[6] Matthias Hoffman,[3] Andrei Kamalov,[1,3] Kirk A. Larsen,[1,3] Siqi Li,[3] Xiang Li,[3] Ming-Fu Lin,[3] Razib Obaid,[3] Philipp Rosenberger,[8,9] Peter Walter,[3] Thomas J. A. Wolf,[1,3] Jon P. Marangos,[5] Matthias F. Kling,[1,2,3] Philip H. Bucksbaum,[1,2,3] Agostino Marinelli,[1,3,‡] and James P. Cryan[1,3,§]

[1]*Stanford PULSE Institute, SLAC National Accelerator Laboratory, Menlo Park, California 94025, USA*
[2]*Department of Applied Physics, Stanford University, Stanford, California 94305, USA*
[3]*SLAC National Accelerator Laboratory, Menlo Park, California 94025, USA*
[4]*Institute of Theoretical Physics, Faculty of Mathematics and Physics, Charles University, Prague, Czech Republic*
[5]*Blackett Laboratory, Imperial College London, London, United Kingdom*
[6]*National Research Council of Canada, Ottawa, Ontario, Canada*
[7]*Department of Physics, Ohio State University, Columbus, Ohio 43210, USA*
[8]*Physics Department, Ludwig-Maximilians-Universität, Munich, Garching, Germany*
[9]*Max Planck Institute of Quantum Optics, Garching, Germany*
[10]*James R Macdonald Laboratory, Kansas State University, Manhattan, Kansas 66506, USA*
[11]*Physics Department, University of Connecticut, Storrs, Connecticut 06269, USA*

(Received 13 June 2024; accepted 4 November 2024; published 16 January 2025)

The detailed understanding of electronic coherence in quantum systems requires measurements on the attosecond timescale. Attosecond x-ray pulses enable the study of electronic coherence in core-excited molecular systems. Here we report on the coherent motion of electrons in the 1,1-difluoroethylene ion following ionization of the K shell of the two nonequivalent carbon sites with a subfemtosecond x-ray pulse. Using the angular streaking technique to track the Auger-Meitner decay, we observe temporal modulations of the emission, indicating the electronic coherence of the core-excited ionic states, and extract a 6.5 ± 0.8 fs average lifetime of the core-level vacancies. A quantum-mechanical model is employed to interpret the measurement, and we find the observed temporal modulations are independent of charge density oscillations. This work opens a new regime of coherent electronic motion, beyond charge migration, where electronic coherence manifests in the nonlocal quantum correlation between atomic sites while charge density oscillation is absent. Our results broaden the landscape of electronic coherence in molecular systems.

DOI: 10.1103/PhysRevX.15.011008 Subject Areas: Atomic and Molecular Physics

I. INTRODUCTION

The direct observation of coherent electronic motion is now possible given recent advancements in attosecond x-ray technology [1–5]. Many important processes, such as solar light harvesting and DNA damage in living cells, are initiated by the interaction of light with matter [6,7]. This light-matter interaction, in which energy is transferred to the electrons in a system, can produce exotic states of matter that can only be described by quantum properties such as coherence and entanglement. Although these states typically exist on extremely short timescales, their properties may have a fundamental effect on the final outcome of the process, such as the generation of a photocurrent or the breaking of a chemical bond.

Coherently populating a superposition of electronic excited states initiates ultrafast electron motion resulting from the interference between the quantum states. One notable method for creating such a superposition state in molecular systems is ionization by broad coherent bandwidth, short-wavelength radiation. The evolution of such superposition states is typically accompanied by the

*Contact author: junwang9@stanford.edu
†Contact author: tdriver@stanford.edu
‡Contact author: marinelli@slac.stanford.edu
§Contact author: jcryan@slac.stanford.edu

Published by the American Physical Society under the terms of the Creative Commons Attribution 4.0 International license. Further distribution of this work must maintain attribution to the author(s) and the published article's title, journal citation, and DOI.

migration of electric charge, which is exemplified by oscillations in the electronic density due to the beating between electronic states [8,9]. This interpretation has successfully described many previous measurements [10–13]. Notably, these previous measurements have all studied superposition states involving valence electrons, whose orbitals are highly delocalized and thus exhibit interference effects across the entire spatial extent of a molecule.

In the x-ray domain, the interaction of a molecule with subfemtosecond pulses produces superpositions between states that involve core-level vacancies [14,15]. In the case of ionization, the superposition will exist between ion-electron pairs. A high degree of coherence in the ion can be achieved using broad bandwidth x-ray pulses to produce significant overlap in the associated photoelectron wave functions [16,17]. For core-level electrons, the binding energy is dependent on screening from the other electrons which bind the molecule, and when an x-ray pulse has sufficient bandwidth to span the energy difference (or "chemical shift") between core-level orbitals, the interaction can now form a superposition between states with core-level vacancies at different atomic sites [18]. Core-level orbitals are typically highly localized around specific atomic sites, except for several atypical cases of systems with a very high degree of symmetry [19,20]. One intriguing consequence of this localization is that the contrast of electronic density modulation produced by a superposition of core vacancies at different atomic sites is expected to be very low. This raises the possibility of coherent electron motion in the absence of charge migration, and leads to the following question: How can electronic coherence be observed experimentally in the near absence of charge density oscillations?

To this end, we probe the electronic coherence created by carbon K-shell ionization of 1,1-difluoroethylene (CH_2CF_2), which has two nonequivalent carbon sites, C_F and C_H, with a K-shell binding energy difference of $\Delta I_C = 4.77$ eV [21,22]. We employ angular streaking [14,23] to measure the time-domain behavior of the Auger-Meitner (AM) emission from the core-excited ion. The angular streaking technique has been used to observe quantum beats in the temporal profile of AM emission [14]. In contrast to the previous study, which exhibited large charge density oscillations, we produce a coherence between core-ionized states that exhibits little to no charge density oscillation. The present work is also differentiated from the previous study by the excitation process: While the previous work considered resonant excitation of a neutral molecule, in this work we prepare a partially coherent ionic state through core-level ionization. This offers an additional layer of complexity to our study: The evolution of the superposition state is now affected by the entanglement between the ion a nd the photoelectron [17,24–26]. Moreover, in this work, the interference with a direct double-ionization process is negligible, which allows us to focus on the coherence between the two core-vacancy states.

Angular streaking employs a circularly polarized infrared (IR) pulse to modify the momentum of electrons depending on the phase of the IR field when they emerge into the continuum. The effect of the IR field can be understood from a semiclassical point of view: The electron momentum shift induced by the IR field with vector potential $\boldsymbol{A}(t)$ is $\boldsymbol{p} - \boldsymbol{p}_0 = e\boldsymbol{A}(t_0)$, where $\boldsymbol{p}$ is the final momentum measured at the detector, when the IR pulse has fallen to zero, $\boldsymbol{p}_0$ is the momentum of the electron at the emission time t_0, and $e < 0$ is the charge of the electron [27,28]. The direction of the IR vector potential rotates at angular frequency ω_L, mapping the emission time to a momentum shift (also referred to as the "streaking" shift) which encodes the time-dependent AM electron emission profile in the measured electron momentum distribution [14,23,29]. Experimentally, we seek to measure the final AM electron momentum distribution as a function of the IR phase at the arrival time of the attosecond x-ray pulse $\omega_L t_i$. We achieve this by sorting the laser shots by $\omega_L t_i$, which we measure on a single-shot basis. The photoelectrons from K-shell ionization are emitted on a timescale much shorter than the IR period and thus experience a collective momentum shift of $e\boldsymbol{A}(t_i)$. As the AM emission persists over a longer timescale, comparable to the IR period, the streaking effect on the AM distribution is more complex [29]. To picture how the t_i-dependent momentum distribution encodes the temporal behavior of AM emission, it is easier to focus on a single final AM momentum $\boldsymbol{p}_a$. Many pathways of the composite system can end with $\boldsymbol{p}_a$. Among these pathways, there is a range of initial electron momenta $\boldsymbol{p}_0(t_0) = \boldsymbol{p}_a - e\boldsymbol{A}(t_0)$ corresponding to different AM emission times t_0. The AM emission delay $\tau = t_0 - t_i$ of each pathway depends on the x-ray arrival time relative to the IR field, since $\boldsymbol{p}_0(t_0)$ is independent of the x-ray arrival time. This means that the t_i-dependent momentum distribution is an informative observable on the delay dependence of the AM emission.

II. EXPERIMENTAL RESULTS

We tune isolated attosecond pulses with ∼0.44 fs duration to a photon energy of ∼374 eV to ionize electrons from the carbon K shell of CH_2CF_2 molecules in the presence of an IR pulse (6.2 fs period, ∼70 fs duration, 0.7 TW/cm^2 average intensity). Since the x-ray pulses are produced by an x-ray free-electron laser (XFEL), they suffer from spectral intensity jitter, which can be quantified with a Fresnel zone-plate spectrometer [30], revealing an average single-shot pulse bandwidth of $\Delta\omega = 5.6$ eV [full width at half maximum (FWHM)]. The ionization from the carbon K-shell orbitals produces an ion-photoelectron pair, initiating the AM process where a second electron emerges in the continuum, as shown in Fig. 1(b). Electrons are collected using a coaxial velocity map imaging spectrometer (c-VMI) [31], as shown in Fig. 1(a). The projection of the emitted electron momentum distribution along the x-ray

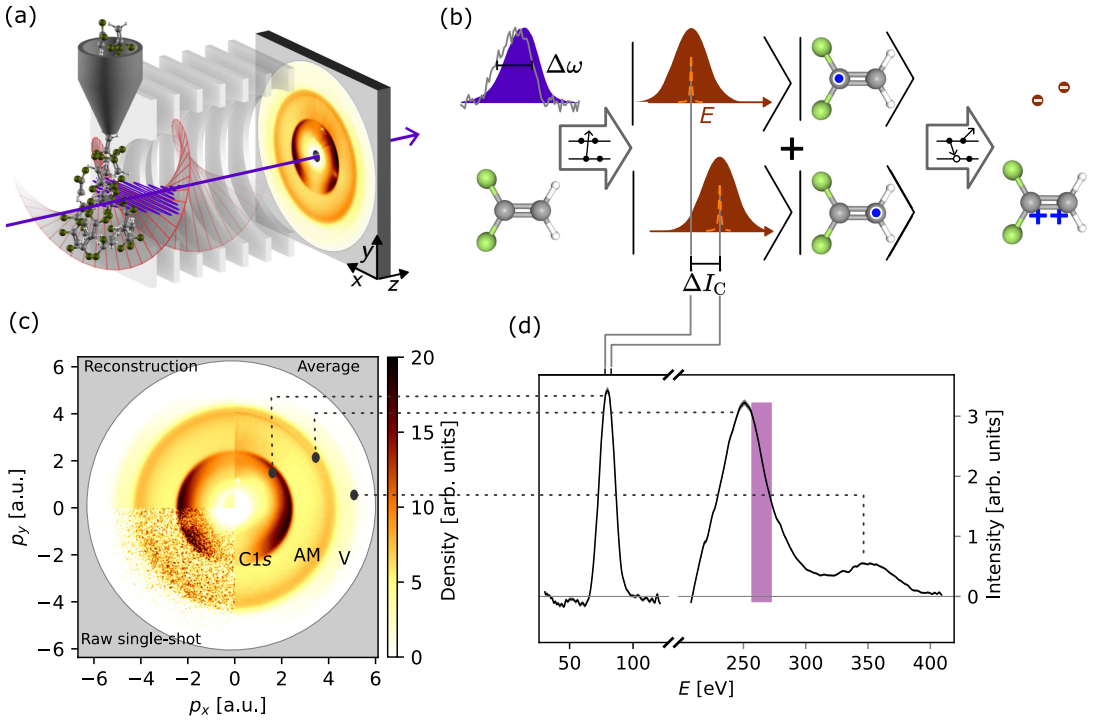

FIG. 1. Overview of the measurement. (a) Copropagating x-ray (purple) and circularly polarized infrared (IR, red) pulses intersect with molecular beam of CH_2CF_2. Emitted electrons are collected by a c-VMI. (b) Schematic of the carbon K-edge photoionization plus Auger-Meitner (AM) decay process. The average x-ray spectrum (blue shade), an example single-shot spectrum (gray trace), and the average pulse bandwidth $\Delta\omega$ (black bar) are shown on the left. The two photoelectron spectra (brown) associated with the core vacancies (blue dots with white outline) are offset in energy by ΔI_C, the energy spacing between cationic states, which is larger than the natural linewidths (orange dashed curves). (c) Projection of electron momentum distribution in the x-ray–IR mistimed case [atomic unit (a.u.)]. Right-hand half is the experimentally measured average. Top left is the reconstructed projection of Abel inversion. Bottom left is an example single-shot image. (d) Kinetic energy spectrum from Abel inversion showing three features: carbon K-shell photoelectrons (C1s), AM electrons, and valence orbital photoelectrons (V). Purple shade corresponds to the ROI for the IR-dressed AM electrons; also see Fig. 2(b).

propagation direction is shown in Fig. 1(c), for the case where the IR field is intentionally mistimed from the x-ray pulse. We clearly resolve three features in the image: photoelectrons emitted from the carbon K shell (C1s), carbon KLL AM emission, and photoelectrons ionized from the valence orbitals (V). The ∼79 eV C1s photoelectrons can be distinguished from the ∼250 eV AM electrons. While the c-VMI energy resolution is sufficient to resolve the 4.77 eV splitting between the C1s^{-1} core-excited cationic states (see Appendix A), the broad bandwidth of the ionizing x-ray pulse causes the K-shell photoelectrons to overlap in kinetic energy and appear as a single feature in Fig. 1(d). This energetic overlap between photoelectrons associated with different ionic states is a prerequisite for suppressing the entanglement and enhancing the degree of coherence in the ion [32].

The large timing jitter between the x-ray and IR pulses [33] necessitates a single-shot measurement of $e\boldsymbol{A}(t_i)$. This quantity can be extracted from the momentum shift of the C1s photoelectrons since the photoemission delay is negligible (<10 as). We employ a cross-correlation approach to measure this shift for x-ray pulses that are cotimed with the IR laser (see Appendix B 1), quantifying the angle $\kappa = \omega_L t_i$ between the momentum shift and the $+x$ direction for each shot. This single-shot tagging approach avoids the need for carrier-envelope phase stabilization of the many-cycle laser pulse. We sort the shots into 40 equally spaced frames according to κ. Figures 2(a)–2(c) present three different frames of the differential momentum distribution (DMD) of all electrons, referenced to the IR-mistimed case, which shows a clear displacement of the C1s feature in the κ direction. The full κ-sorted result is presented in Supplemental Material Video S1 [34]. The valence feature is displaced in nearly the same direction as the C1s feature, indicating that the valence photoelectrons are also emitted almost instantaneously with respect to the laser period.

We analyze a region of interest (ROI) of the DMD indicated by the purple ring in Fig. 2(b), on the high-energy side of the AM feature. This ROI is divided into angular bins labeled by the angular position θ on the detector plane. We define $Y_{\mathrm{AM}}(\theta,\kappa)$ to be the differential AM yield in the θ bin, i.e., the change in AM yield induced by the streaking

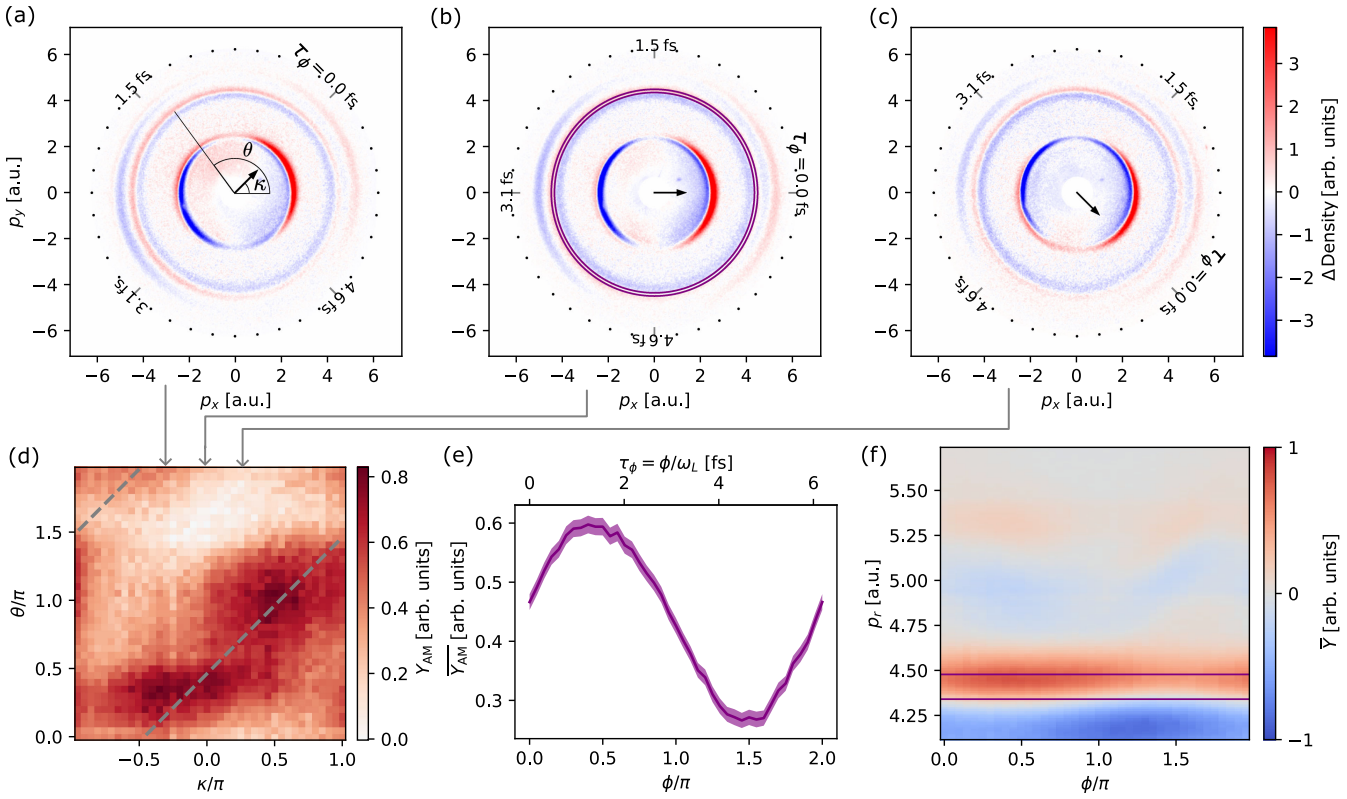

FIG. 2. Effect of the streaking laser on the AM distribution. (a) Measured differential momentum distribution (DMD) for the frame when the C1s momentum shift direction (black arrow) is $\kappa = +\pi/4$. The peripheral ticks on the clock face label the effective delay $\tau_\phi \equiv \phi/\omega_L \equiv (\theta - \kappa)/\omega_L$. (b),(c) Same as (a) but with streaking directions $\kappa = 0$ and $\kappa = -\pi/4$, respectively. The color bar in (c) applies to (a)–(c). (d) Measured differential AM yield in the ROI specified by the purple ring ($4.34 < p_r < 4.48$ a.u.) in (b), with the valence background subtracted. Panels (a)–(c) correspond to three columns. The dashed line follows $\theta - \kappa = 0.46\pi = 1.45$ rad. (e) The delay-invariant average of (d) $\overline{Y_{\mathrm{AM}}}(\phi)$ (solid line), with the shaded area representing $\pm 2\times$ standard error of the mean ($\sigma_{\bar{x}}$). (f) Measured DMD of AM electrons after the valence subtraction and the delay-invariant averaging $\bar{Y}(\phi, p_r)$. The ROI in (b) is marked by solid lines.

effect, for the frame labeled by the κ direction. The measured $Y_{\mathrm{AM}}(\theta, \kappa)$ is shown in Fig. 2(d), following the removal of a weak background contribution from the valence photoelectrons. At ~ 374 eV photon energy, the valence photoelectrons are well above the AM electrons in KE [35,36]. Therefore we characterize the contribution from the valence photoelectrons using the measured valence feature in a separate detector region at higher kinetic energy than the ROI for AM (see Appendix B 5). The positive ridge around the $\theta - \kappa \approx 1.45$ rad line arises from the delay between the C1s photoemission and the AM emission.

For each angular bin, the relative angle $\phi = \theta - \kappa$ corresponds to an effective delay $\tau_\phi = \phi/\omega_L$ referenced to the C1s photoionization process. This effective delay τ_ϕ is labeled in Figs. 2(a)–2(c). For the AM yield in a single θ bin, the series of κ frames corresponds to a series of effective delay points. The correspondence between κ frame and effective delay changes between each θ bins, according to $\tau_\phi = (\theta - \kappa)/\omega_L$. Therefore we average the measured Y_{AM} over $N_\theta = 36$ angular bins according to

$$\overline{Y_{\mathrm{AM}}}(\phi) = \frac{1}{N_\theta} \sum_{q=1}^{N_\theta} Y_{\mathrm{AM}}(\theta_q, \theta_q - \phi), \tag{1}$$

obtaining the signal shown in Fig. 2(e). This averaging, which we refer to as the delay-invariant averaging, is useful, because in the absence of angular correlation between the AM-electron and photoelectron emission in the laboratory frame, the dependence of $Y_{\mathrm{AM}}(\theta, \theta - \phi)$ on ϕ is equivalent for all θ bins. Considering a momentum region far above the IR-free AM feature, the effective delay τ_ϕ can be interpreted as the AM delay τ. We also calculate the delay-invariant average of the DMD of AM electrons for different bins in radial momentum p_r, $\overline{Y}(\phi, p_r)$, as shown in Fig. 2(f).

A. Core-vacancy lifetime

The lifetime of the core-level vacancy is an important aspect of the electronic motion, since such population decay will damp any potential coherence. The slow variation of $\overline{Y_{\mathrm{AM}}}(\phi)$ shown in Fig. 2(e) with a characteristic

frequency of ω_L is sensitive to the average lifetime of the two C1s^{-1} ionic states. To describe the measurement we adapt the quantum-mechanical model introduced in Refs. [29,37] to the case of multiple core-ionization channels emitting coherently, which is illustrated in the diagram in Fig. 3(a) and detailed in Sec. III. The interaction with IR dressing field is treated in the strong-field approximation (SFA), and the AM emission is treated as a coherent concerted process [29,38]. Owing to the periodic nature of ϕ, our signal decomposes into discrete Fourier components, with complex coefficient $H_m = \int_0^{2\pi} \overline{Y_{\mathrm{AM}}}(\phi) e^{-im\phi} d\phi/(2\pi)$ associated with mode $e^{im\phi}$. These modes correspond to the harmonics of the IR frequency $m\omega_L$, and the slow variation is characterized by the $m = 1$ mode. As shown in Fig. 3(c), comparing to the simulation, we extract the average lifetime of the core vacancies as $\Gamma^{-1} = 6.5 \pm 0.8$ fs, consistent with results from *ab initio* calculations (see Appendix D). The SFA calculation for a 6.5 fs lifetime agrees with the measured signal $\overline{Y_{\mathrm{AM}}}(\phi)$, whereas a shorter lifetime of 2 fs leads to a notable discrepancy, Fig. 3(b). We choose 2 fs for comparison because it represents a lower limit obtained from a linewidth measurement [39], assuming the absence of vibrational structure.

B. Quantum beat in Auger-Meitner emission

In addition to the oscillation at the IR laser frequency, we observe higher-frequency modulations of the measured AM signal. Among the higher ($m > 3$) Fourier component amplitudes, we find evidence for a peak at $m = 7$, as shown in Fig. 4(a). The Hotelling's test [40] reveals that the measured H_7 is significantly nonzero (p value <0.05), unlike the neighboring coefficients (H_5, H_6, H_8, and H_9). Therefore the dominant component in the high-frequency modulation is the oscillation at $7\omega_L$, which is very close to the energy spacing $\Delta I_{\mathrm{C}} = 7.1\hbar\omega_L$.

This modulation reflects the quantum beat in the instantaneous AM emission rate, which can be understood as the interference between many two-electron (photoelectron and AM-electron) emission pathways. As illustrated in Fig. 3(a), the AM process proceeds *via* intermediate states, characterized by a core vacancy in one of the nonequivalent carbon sites and a photoelectron. The interference between these pathways is observed when the final three-body state (photoelectron, AM electron, and dication) is the same. The broad bandwidth of the x-ray pulse produces overlap in the photoelectron momentum. In the absence of the IR field, the AM emission to a common dicationic state can be resolved, since the energy spacing $\Delta I_{\mathrm{C}} = 4.77$ eV is much larger than the natural linewidth [39]. However, as illustrated in Fig. 3(a), in the presence of the IR field, the pathways with AM emission times t_1 and t_2 from the respective C1s^{-1} states can arrive at a common final $\boldsymbol{p}_a$. The relative phase between the two pathways accumulates according to the total energy difference ΔI_{C} of

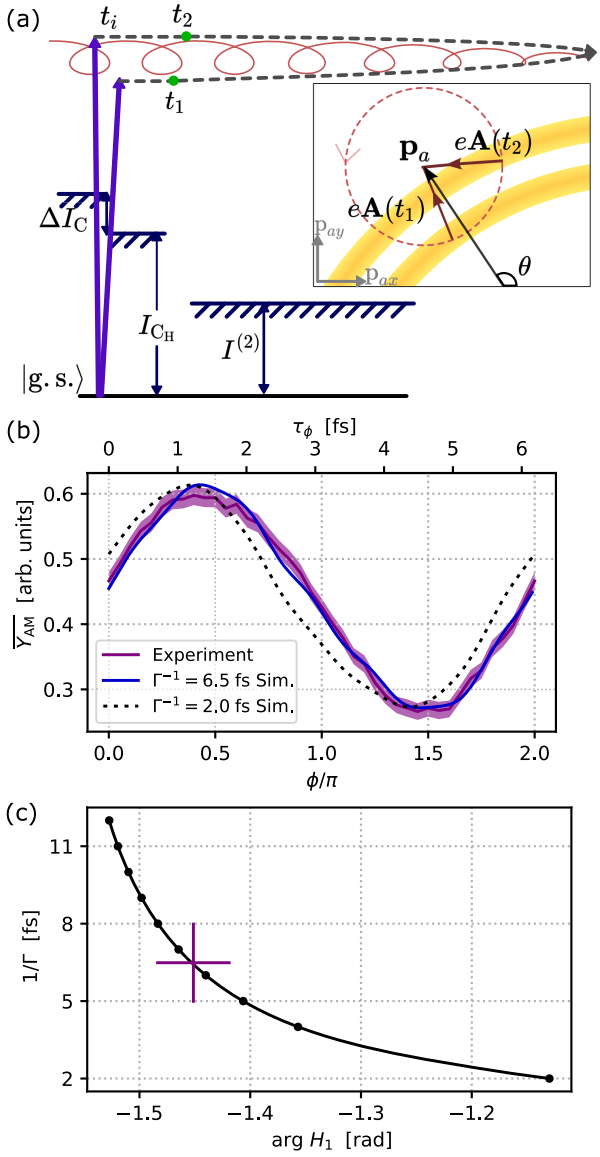

FIG. 3. Lifetime estimation of the C1s^{-1} core-excited ionic states. (a) Diagram of the model for dressed AM emission as a sum over pathways. In each pathway, the time evolution (gray dashed line) begins with photoionization (blue arrow) of the molecular ground state (g.s.), followed by an AM transition (green dot), in the presence of the IR field (red solid line). Two example pathways proceed via different carbon core vacancies. Inset shows a semiclassical picture in AM electron momentum space. The yellow arcs show a magnified view of the IR-free AM spectrum for a pair of AM channels sharing a single dicationic state. The semiclassical range of initial momenta (red dashed line) for the final momentum $\boldsymbol{p}_a$ depends on the IR vector potential at the emission time (brown arrow). (b) Delay-invariant average of the differential AM yield calculated with the coherent model for core-vacancy lifetime of 6.5 fs (blue solid line) and 2.0 fs (black dotted line), compared to the measurement [purple; same as Fig. 2(e)]. (c) Calculated phase of the first Fourier coefficient H_1 for various lifetimes (black dots), with a cubic-spline interpolation (black solid line). The purple cross marks the measured phase horizontally and the retrieved lifetime vertically, with the error bars representing $\pm 2\sigma_{\bar{x}}$ of the respective quantities.

the intermediate ion-electron pairs, leading to a modulation of the final-state population at the beat frequency of $\Delta I_C/h$. We attribute the high-frequency oscillation to a quantum beat with a period of 900 as, which arises from the electronic coherence between the two $C1s^{-1}$ states of $CH_2CF_2^+$.

III. MODEL

We model the AM emission as a correlated process, and the interaction with IR dressing field is treated within the SFA [29,38]. The measured AM distribution is modeled by tracing over the photoelectron momentum $\boldsymbol{p}_p$ space while resolving the AM electron momentum $\boldsymbol{p}_a$, since we do not discriminate on $\boldsymbol{p}_p$ in our measurement:

$$\rho_A(\boldsymbol{p}_a) = \int d^3\boldsymbol{p}_p |b_F(\boldsymbol{p}_a,\boldsymbol{p}_p) + b_H(\boldsymbol{p}_a,\boldsymbol{p}_p)|^2. \quad (2)$$

Here $b_\alpha(\boldsymbol{p}_a,\boldsymbol{p}_p)$, $\alpha = F, H$ describes the final-state amplitude associated with a particular intermediate core vacancy at the C_α site:

$$b_\alpha(\boldsymbol{p}_a,\boldsymbol{p}_p) = M_\alpha \int_{-\infty}^{\infty} dt e^{iS(t,\boldsymbol{p}_a)-i(I_\alpha-I^{(2)})t/\hbar} \int_{-\infty}^{t} dt_i e^{i(E_p+I_\alpha)t_i/\hbar-\Gamma(t-t_i)/2} D_\alpha(\boldsymbol{p}_p) E_X(t_i), \quad (3)$$

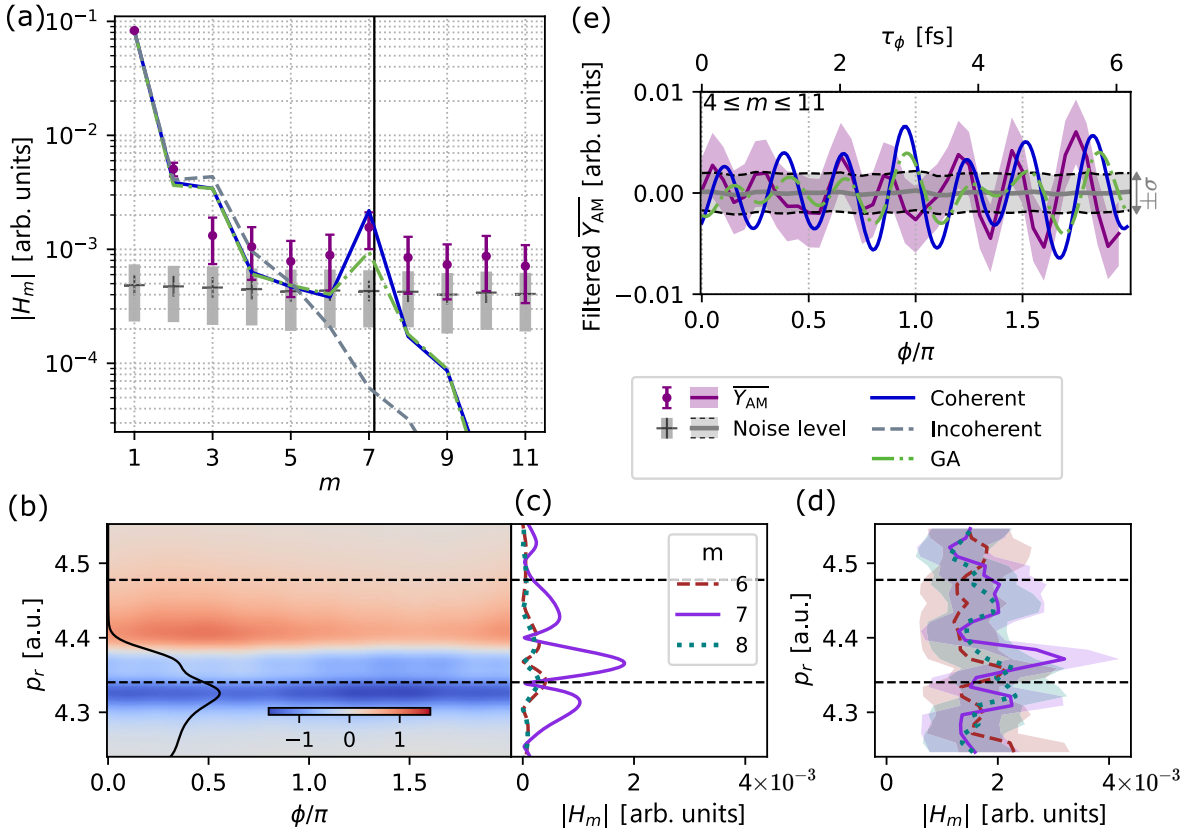

FIG. 4. Electronic coherence in core-excited ionic states. (a) Fourier coefficient amplitudes of the measured $\overline{Y_{AM}}(\phi)$ (purple dots). Lines show results from simulations with the coherent model (blue solid line), fully incoherent model (gray dashed line), and the geometry averaged model (green dot-dashed line). All three models are normalized to minimize the rms error on $\overline{Y_{AM}}(\phi)$ from the measurement. The measured noise level (gray crosses; see Appendix B 2) is shown for each coefficient. Vertical solid line marks $\Delta I_C/\hbar\omega_L$. (b) Calculated delay-invariant average of the DMD of AM electrons, along with the radial profile of the IR-free distribution (black solid line). (c) Momentum-resolved Fourier coefficient amplitudes of the simulated map in (b). (d) Momentum-resolved Fourier coefficient amplitudes of the experimentally measured $\overline{Y}(\phi, p_r)$ in Fig. 2(f). (e) Comparison of the quantum beat after Fourier filtering the delay-resolved measurement (purple) and simulations in the band of $4 \le m \le 11$. The measured noise level is filtered in the same way and presented in gray. The filtered simulation results follow the same legends as in (a). The error bars and shaded areas represent $\pm\sigma_{\bar{x}}$. The ROI (dashed line) in (b)–(d) is the same as in Fig. 2.

where $S(t,\boldsymbol{p}) = \int_{-\infty}^{t} d\tau[\boldsymbol{p} - e\boldsymbol{A}(\tau)]^2/(2m\hbar)$ is the Volkov phase, I_α is the ionization potential associated with the $C_\alpha 1s^{-1}$ state, $E_p \equiv \boldsymbol{p}_p^2/(2m)$ is the photoelectron kinetic energy (in the absence of IR field), M_α is the AM transition matrix element, $D_\alpha(\boldsymbol{p}_p)$ is the component of the transition dipole along the x-ray pulse electric field $E_X(t)$, and $1/\Gamma$ is the core-vacancy lifetime (due to all decay channels). This model considers a single dication final state with an energy $I^{(2)}$ that is adjusted to match the experiment. Equation (2) assumes full coherence for the multielectron system, so we refer to this as the coherent model. After tracing over the outgoing photoelectron, the complementary system, consisting of the dication and the AM electron, is in a partially coherent state. We use this coherent model to estimate the core-vacancy lifetime in Fig. 3. The x-ray bandwidth $\Delta\omega$ and the energy spacing $\Delta I_C = I_F - I_H$ are taken from the experiment. The simulated ρ_A is projected along z, blurred according to the experimental resolution and then averaged according to the measured distribution of $|e\boldsymbol{A}(t_i)|$, as detailed in Appendix C. The derivation of Eq. (3) is provided in Sec. I of Supplemental Material [34].

As shown in Fig. 4(a), the coherent model ("Coherent," blue solid line) generally agrees with the measured Fourier component amplitudes. When we remove the possibility of coherence between the core-ionized states, i.e., we omit $b_F^* b_H + b_H^* b_F$ in Eq. (2), the peak at $m = 7$ vanishes as shown in Fig. 4(a) ("Incoherent," gray dashed line). This further supports our assignment of the peak at $m = 7$ to quantum coherence in the core-ionized states. We have also simulated the situation where the x-ray bandwidth is broadened to $\Delta\omega \gg \Delta I_C$, preparing a nearly pure superposition (purity > 0.96) in the cation; see Supplemental Fig. S3 [34]. In this case, the simulated amplitude $|H_7|$ is larger than what is shown in Fig. 4(a) and less consistent with the measurement.

Modeling the projected electron momentum distribution we calculate the momentum-resolved DMD and its dependence on the effective delay τ_ϕ, Fig. 4(b). The positive variation on the high-energy side of the momentum distribution, which is more pronounced at $\phi < \pi$, is in agreement with the experimental result shown in Fig. 2(f). This DMD allows us to perform the same Fourier analysis shown in Fig. 4(a), for different bins of radial momentum p_r. The resultant momentum-resolved Fourier spectrum of the simulated signal is shown in Fig. 4(c). The prominent $m = 7$ component shows a main peak and two side lobes. We apply the same procedure to our experimental data, shown in Fig. 4(d), and observe qualitative agreement with our simulation.

In contrast to previous work probing coherence between core-excited states with the same electronic configuration [14], in this work we probe the coherence between states with a core vacancy at different atomic sites. One consequence of the energetic splitting between the $C_\alpha 1s^{-1}$ states is that the kinetic energies of the AM electrons associated with the same dicationic state are well separated in the IR-free case. We therefore choose the experimental ROI to be lower than the high-momentum edge, in order to capture significant amplitude from the lower-energy AM channels associated with the C_H core vacancy.

The measurement and simulation of the AM modulation are further compared by applying a bandpass Fourier filter ($4 \le m \le 11$) to the delay-dependent AM yield $\overline{Y_{AM}}(\phi)$, as shown in Fig. 4(e). The oscillation in the coherent model has a similar magnitude as the measurement, but it presents a notable discrepancy in the phase. The measured oscillation at $7\omega_L$ has a phase of $\arg H_7 = -0.9 \pm 0.5$ rad whereas the coherent model predicts a phase of -2.15 rad. To better understand the time-domain behavior, we explore the molecular geometry dependence of the energy difference between the $C1s^{-1}$ states. We average over an ensemble of 1000 geometries sampled from the vibrational ground state of the molecule to account for the quantum-mechanical spread of the wave packet [41]. This geometry averaged (GA) (green dot-dashed line in Fig. 4) model is shown along with the measurement and the coherent model in Figs. 4(a) and 4(e). The peak at $m = 7$ persists in the presence of geometry averaging, but the discrepancy in the phase of the oscillation is not resolved. Rather, the effect of molecular geometry averaging is to suppress the contrast of the oscillation, indicating a reduction of coherence. We note there is a discrepancy between the measurement and any of the models presented in Fig. 4(a) for the amplitude $|H_3|$. Given the persistence of $|H_3|$ in the incoherent model, it is clearly not related to the electronic coherence, rather this discrepancy likely reflects the limitation of considering only a single dicationic state.

IV. DISCUSSION

We also explore the effect that the relative phase between the final-state amplitudes, b_F and b_H, has on the time-domain signal in Fig. 4(e). Such a phase shift would correspond to the phase between the AM transition matrix elements (M_H and M_F) that describe the decay of the core-ionized state to a common dicationic state. Adjusting the phase $\arg H_7$ by changing the relative phase of the AM matrix elements in our model to agree with our measurement results in an overall degradation in agreement for the full time-domain signal, as shown in Sec. I.6 of Supplemental Material [34]. Thus a relative phase shift cannot resolve the discrepancy in Fig. 4(e). Our SFA models (coherent and GA) omit several mechanisms which may affect the phase of the quantum beat. For instance, the models do not include the motion of the nuclear wave packets on the two $C1s^{-1}$ potential energy surfaces, which can modify the phase of the electronic coherence [42]. We use the semiclassical model [42] described in Appendix E to estimate the impact of the centroid motion of the nuclear wave packet in our measurement. We calculate a dephasing time of 4 fs, which is likely to be an underestimate since this semiclassical approach ignores the dispersion of the nuclear wave packets. Additionally, the phase of the coherent oscillation could be sensitive to

nonadiabatic coupling between the electronic and nuclear degrees of freedom [43], the population of shakeup states in photoionization, the decay of the system to multiple dicationic states, and the anisotropy of the AM electron emission, all of which are also absent from our model.

As pointed out above, the measured quantum beat in the AM emission directly results from the coherence between the two core-ionized states. Such coherence can be formally described using the reduced ionic density matrix (R-IDM) $R_{\alpha\alpha'}(t)$ in the space of the two $C_\alpha 1s^{-1}$ cationic states, which are eigenstates of the bound $N-1$ electron system. This R-IDM consists of the population of the core-excited states (R_{HH} and R_{FF}) and the coherence between them (R_{HF}). According to Eq. (3), the interference in AM emission $\int d^3\boldsymbol{p}_p b_{\mathrm{H}} b_{\mathrm{F}}^*$ is mapped from the coherence R_{HF} by the AM transitions, scaling with $M_{\mathrm{H}}M_{\mathrm{F}}^*$, as shown in Appendix C. The interference relies on both $C1s^{-1}$ states being coupled to the same dicationic state by the interaction within the multielectron system.

Typically, coherence gives rise to oscillations in electronic density, which is described by the diagonal elements ($\boldsymbol{r}_1 = \boldsymbol{r}_2$) of the electronic single-body reduced density matrix (1-RDM):

$$\rho(\boldsymbol{r}_1, \boldsymbol{r}_2, t) = \sum_{n,m} \varphi_n^*(\boldsymbol{r}_1)\rho_{nm}^{\mathrm{orb}}(t)\varphi_m(\boldsymbol{r}_2), \tag{4}$$

where $\{\varphi_n\}$ is a basis of molecular orbitals and $\rho_{nm}^{\mathrm{orb}}(t)$ is the electronic 1-RDM in the orbital representation [32,44]. Equation (4) is defined for a general pair of positions $\boldsymbol{r}_1$ and $\boldsymbol{r}_2$. The 1-RDM of the vacancy (or "hole 1-RDM") is given by $\Delta\rho \equiv \rho_{\mathrm{g.s.}} - \rho$, the difference between the molecular ground state and the ion. Since the $C1s^{-1}$ states are well described by the *removal* of an electron from the carbon core orbitals $\varphi_\alpha, \alpha = \mathrm{H}, \mathrm{F}$, we have $\Delta\rho(\boldsymbol{r}_1, \boldsymbol{r}_2, t) \approx \sum_{\alpha,\alpha'} \varphi_\alpha^*(\boldsymbol{r}_1)R_{\alpha\alpha'}(t)\varphi_{\alpha'}(\boldsymbol{r}_2)$. The oscillations in charge density arising from the ionic coherence are given by $\varphi_{\mathrm{H}}^*(\boldsymbol{r})\varphi_{\mathrm{F}}(\boldsymbol{r})R_{\mathrm{HF}}(t) + \mathrm{c.c.}$ Notably, in our case this oscillation is heavily suppressed due to the small spatial overlap between the core-level orbitals. However, another spatial manifestation of the coherence is the nonlocal correlation between $\boldsymbol{r}_1 \neq \boldsymbol{r}_2$. In the system considered here, despite the lack of spatial overlap, there is a strong nonlocal correlation between the two carbon sites $\Delta\rho(\boldsymbol{r}_{\mathrm{C_H}}, \boldsymbol{r}_{\mathrm{C_F}}, t) \approx \varphi_{\mathrm{H}}^*(\boldsymbol{r}_{\mathrm{C_H}})R_{\mathrm{HF}}(t)\varphi_{\mathrm{F}}(\boldsymbol{r}_{\mathrm{C_F}})$. Even in the limiting case where the spatial overlap $\varphi_{\mathrm{H}}^*(\boldsymbol{r})\varphi_{\mathrm{F}}(\boldsymbol{r})$ is exactly zero, both this nonlocal correlation and the quantum beat in the AM emission would not vanish. Thus, the measured quantum beat is evidence of coherent electron motion in a fundamentally different regime from charge migration: where the electronic coherence manifests in the time evolution of the spatial quantum correlation, even in the near or complete absence of charge density oscillations.

While the manifestation of electronic coherence in the spatial correlation generally persists in the complete absence of charge density motion, there is a small but finite spatial overlap between the core orbitals considered in our measurement. This results in charge density oscillations with a contrast of roughly 0.3%; a regime we term the "near-absence" of charge density oscillation. We calculate the 1-RDM of the vacancy $\Delta\rho$, which is visualized in Figs. 5(a)–5(c) in terms of the two-dimensional slice along the molecular axis (also see Video S2 in Supplemental Material [34] for the animated version). The 1-RDM is calculated for molecular orbitals from a

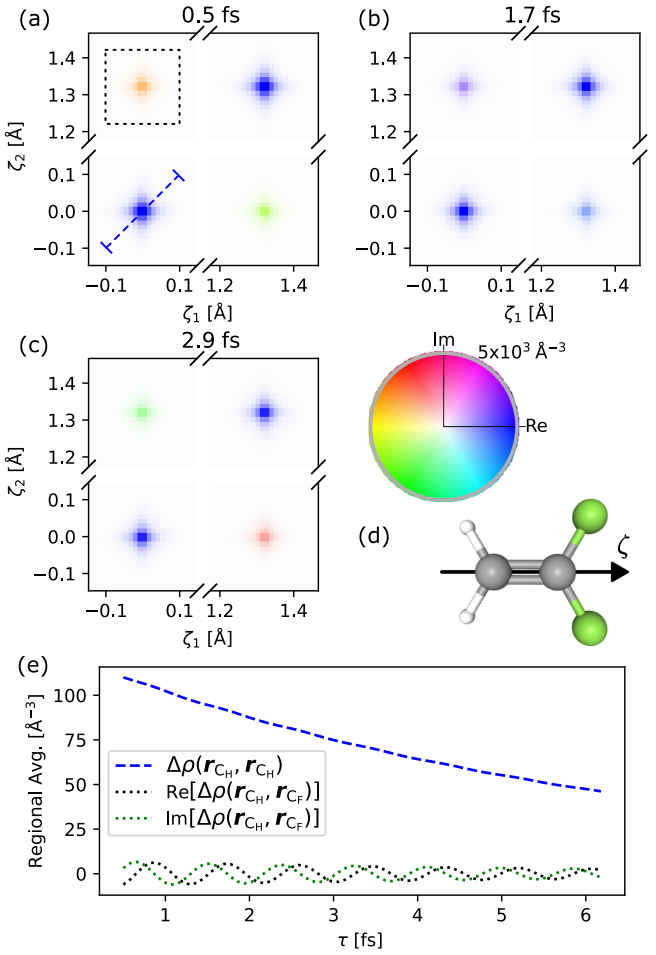

FIG. 5. 1-RDM of the vacancy in the ion $\Delta\rho$ sliced along the symmetry axis ζ of the molecule, shown at three delay instants relative to the x-ray arrival time (a) $\tau = 0.5$ fs, (b) $\tau = 1.7$ fs, and (c) $\tau = 2.9$ fs. The magnitude and phase of the complex values are encoded by the saturation and hue of the color, respectively, as presented by the color wheel in (c). The edge of the wheel marks 5×10^3 Å^{-3}. (d) A schematic of the molecule showing the ζ axis. (e) Volume regional averages of $\Delta\rho$ in the 0.1 Å-radius vicinity of the carbon sites, as functions of the AM delay τ. The hole charge density averaged around the C_H site [blue dashed segment in (a)] is shown by the blue dashed curve. The nonlocal correlation between the two carbon sites, averaged in the dotted box in (a), is shown by the two dotted lines. The real and imaginary parts are shown in black and green, respectively.

restricted Hartree-Fock (RHF) calculation using the aug-cc-pwCVTZ basis set, and $R_{\alpha\alpha'}$ is modeled with the experimentally determined lifetime of 6.5 fs. The initial degree of coherence is set according to the measured $|H_7|$ in reference to the simulation with the coherent SFA model (see Appendix C). The dynamic hole charge at the C_H site $Q_H(t)$ is quantified as the integral of $\Delta\rho(\boldsymbol{r},\boldsymbol{r},t)$ within a sphere of 0.1 Å radius, as shown in Fig. 5(e). The oscillation lying on top of the monotonically decaying dynamic hole charge $Q_H(t)$ shown in Fig. 5(e) is imperceptible, due to its contrast of 3×10^{-3} (ratio of the oscillation amplitude to Q_H). The nonlocal correlation, on the other hand, demonstrates high-contrast oscillations at the frequency of $\Delta I_C/h$ in both its real and imaginary parts, as shown in Fig. 5(e). The oscillation in the nonlocal correlation results from the relative phase evolution between the multielectron wave function, at the different positions corresponding to the two carbon core orbitals. The mapping of coherence between the ionic states to the interference in the AM emission is mediated by electron-electron interaction, which is independent from the direct spatial overlap $\varphi_H^*(\boldsymbol{r})\varphi_F(\boldsymbol{r})$ that facilitates the charge migration. This electronic coherence could also be probed by mechanisms such as x-ray photoelectron spectroscopy, as proposed in Ref. [18].

In summary, we report the measurement of coherent electron motion in a superposition of core-level vacancies at different atomic sites in CH_2CF_2 molecules. We observed a modulation of the AM emission with a 0.9 fs period. This is driven by partial coherence of the ion in an entangled ion-photoelectron pair produced by broad bandwidth x-ray pulses. We interpret our experiment with a quantum-mechanical model of the AM emission in the presence of a streaking field. Our model supports the interpretation that coherent electron motion is driven by a superposition of core-ionized states with core-level vacancies at different atomic sites. This represents the regime where coherent electron motion can be embodied in the spatial quantum correlation rather than in charge density oscillation. The interaction within the multielectron system plays a crucial role in mediating the coherence of the ion to the time dependence of the AM emission. Therefore, using attosecond angular streaking of AM emission, we have been able to probe coherent electron motion in the near-absence of charge migration. In addition to demonstrating quantum correlations in multielectron systems beyond charge density modulation, one intriguing possibility would be to leverage the ion-electron entanglement to select the electronic properties of the cation. By controlling or postselecting the photoelectron properties one could investigate the electronic evolution of the cation under various initial conditions of the coherence.

ACKNOWLEDGMENTS

Use of the Linac Coherent Light Source (LCLS), SLAC National Accelerator Laboratory, is supported by the U.S. DOE, Office of Science, Office of Basic Energy Sciences under Contract No. DE-AC02-76SF00515. This work is primarily supported by the U.S. DOE, Office of Science, Office of Basic Energy Sciences (BES), Chemical Sciences, Geosciences, and Biosciences Division (CSGB). P. L. F., R. R. R., Z. G., D. C., J. D., S. L., and A. M. acknowledge support from the Accelerator and Detector Research Program of the Department of Energy, Basic Energy Sciences division. P. L. F., R. R. R., and Z. G. also acknowledge support from Robert Siemann Fellowship of Stanford University. P. K. acknowledges financial support from the Czech Science Foundation (Project GACR No. 22-22658S). K. B. acknowledges additional support by the U.S. Department of Energy, Office of Science, Office of Workforce Development for Teachers and Scientists, Office of Science Graduate Student Research (SCGSR) program.

T. D., A. M., and J. P. C. devised the experimental scheme. J. W., T. D., P. L. F., M. H., R. O., M. G., and J. P. C. prepared the experimental apparatus. The experiment was performed by J. W., T. D., E. I., Z. G., M.-F. L., R. O., K. A. L., X. C., X. L., S. B., A. K., and J. P. C. The attosecond x-ray pulses were prepared by R. R. R., D. C., J. D., S. L., and A. M. The data analysis was led by J. W. and supported by Z. G., E. I., O. A., and P. R. The modeling was performed by J. W., P. K., and J. P. C. All authors participated in the preparation of the manuscript.

APPENDIX A: EXPERIMENTAL SETUP

Isolated attosecond x-ray pulses (~374 eV central photon energy, 23 μJ average pulse energy, ~0.44 fs FWHM duration, polarized along x direction) were produced by the Linac Coherent Light Source XFEL using the XLEAP configuration [1]. The repetition rate of the XFEL is 120 Hz. The average autocorrelation of the spectra $I(\omega)$ is fitted by a Gaussian function of 7.9 eV FWHM, as shown in Fig. 6(a). This converts to the average pulse bandwidth of $\Delta\omega = 7.9\ \text{eV}/\sqrt{2} = 5.6$ eV FWHM. The pulse duration is estimated from XFEL simulations, consistent with the measured bandwidth and the time-bandwidth product characterized in previous measurements [1,14,45]. The circular polarization of the IR pulses was optimized with an ultrabroadband quarter wave plate to >0.95 ellipticity, according to the above-threshold ionization spectrum of xenon. The residual systematic deviation in the time-angle mapping is negligible (<0.026 rad) compared to the uncertainty in κ (see Appendix B 1). The IR focus is moved away from the interaction point to suppress the Gouy phase averaging and above-threshold ionization. Other details of the IR laser have been reported in Ref. [45].

The CH_2CF_2 target is introduced as a skimmed molecular beam which intersects the copropagating x ray and the IR pulses. The beam is pulsed at the repetition rate of the FEL, controlled by a supersonic gas nozzle (Even-Lavie).

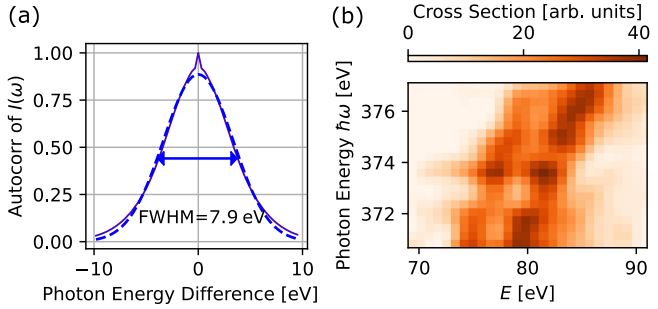

FIG. 6. Characteristics of x-ray pulse and gas target. (a) Autocorrelation of measured x-ray spectral intensity (purple solid line). The average autocorrelation is fitted with a Gaussian function (blue dashed line) of 7.9 eV FWHM. (b) Photon-energy-resolved ionization cross section of the C1s feature, measured in the mistimed case.

The c-VMI design is described in Ref. [31]. In the analysis, we have excluded a window of four angular bins within $1.52 \leq \theta/\pi \leq 1.72$ from the delay-invariant averaging, due to an imaging imperfection in our c-VMI setup. The energy resolution of the c-VMI is sufficient to resolve the 4.77 eV spacing. As shown in Fig. 6(b), the two K edges are resolved in the photon energy-resolved ionization cross section obtained by sequentially applying Abel inversion and spectral regression to the mistimed images [46]. Subbandwidth resolution in photon energy is achieved by leveraging fluctuations in the spectral intensity $I(\omega)$, revealing the c-VMI energy resolution to be $\Delta E/E \sim 3\%$ in this range of KE. The ionization cross section shown in Fig. 6(b) is the linear response of the molecule, rather than any electron spectrum. Therefore the broad bandwidth of the x-ray pulse still leaves the association of individual photoelectrons with individual cationic states indistinguishable.

APPENDIX B: DATA ANALYSIS

1. Single-shot measurement of momentum shift

The single-shot momentum shift of the C1s feature was measured by maximizing the normalized cross-correlation with the average C1s feature measured in the IR-mistimed case [47]. The cross-correlation was first evaluated at the integer-pixel grid points as a matrix, in the range of $|\delta p_x|, |\delta p_y| \leq 0.38$ a.u. (unless stated otherwise). Then for subpixel resolution, we fitted the cross-correlation matrix around the maximal grid point with a quadratic form $(\delta\boldsymbol{p} - \boldsymbol{k})^T H(\delta\boldsymbol{p} - \boldsymbol{k})/2 + r_M$, obtaining the maximal point $\boldsymbol{k} = \arg\max R(\delta\boldsymbol{p}) = e\boldsymbol{A}(t_i)$, the Hessian matrix H, the maximal cross-correlation r_M, and the residual rms error ϵ of the fit. A single-shot example is presented in Figs. 7(a) and 7(b). This procedure demonstrated robustness to the experimental fluctuations (such as x-ray pulse energy fluctuation, counting noise of the electrons). On the intentionally mistimed dataset, the measured streaking shifts are densely concentrated at $\boldsymbol{k} = 0$, as shown in Fig. 7(c). In contrast, on the nominally cotimed dataset, the streaking shifts are in a much broader distribution as expected, Fig. 7(d).

For the nominally cotimed dataset, the streaking shift could be small due to jitter in IR intensity and the IR–x-ray temporal-spatial overlap, so we excluded the insignificantly shifted shots whose uncertainty ellipsoid $-(\delta\boldsymbol{p} - \boldsymbol{k})^T H(\delta\boldsymbol{p} - \boldsymbol{k}) < s^2\epsilon$ covered $\delta\boldsymbol{p} = 0$. The scale factor $s^2 = 1.1$ had been chosen such that 95% of the mistimed shots were considered insignificantly shifted. Discriminating the data in this way produces the distribution shown in Fig. 7(e). The distribution in $|\boldsymbol{k}|$ of the shots in Fig. 7(e) is shown in Fig. 7(f), which converts to an

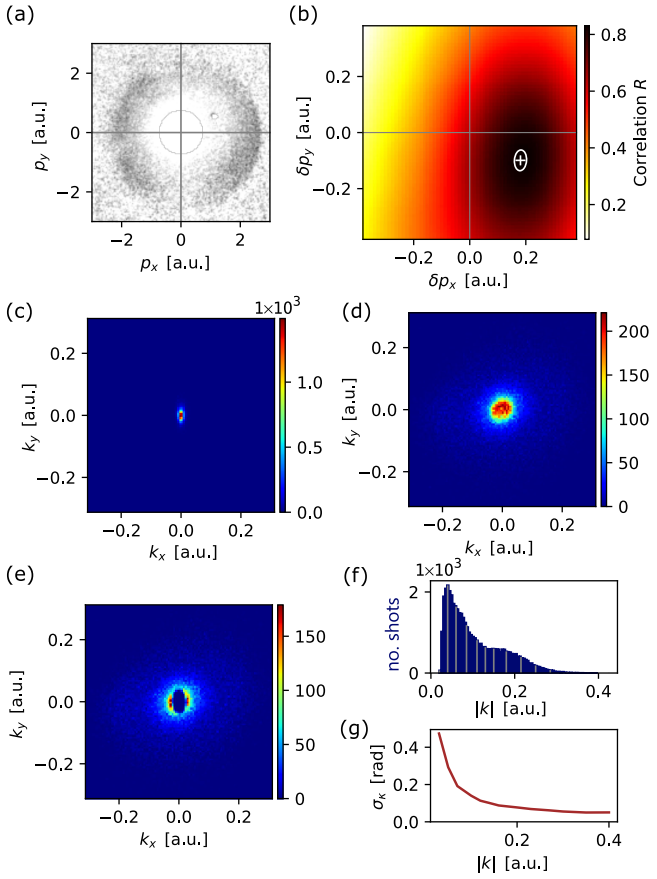

FIG. 7. Measured C1s momentum shifts. (a) C1s feature in an example single shot. (b) Single-shot cross-correlation of the C1s feature in (a) with the measured IR-mistimed distribution, marked with the maximum point $\boldsymbol{k}$ (cross) and the uncertainty ellipsoid. (c)–(e) Distributions of the measured C1s momentum shift $\boldsymbol{k}$ for (c) the intentionally mistimed shots, (d) the nominally cotimed shots, and (e) the significantly shifted cotimed shots. Colors encode number of shots. The standard deviation of the mistimed shots in (c) is 0.008 and 0.018 a.u. in k_x and k_y, respectively. (f) Distribution of the shots in (d) in streaking shift amplitude $|\boldsymbol{k}|$. Areas separated by gray lines are proportional to the weights of each $|\boldsymbol{k}|$ bin in the simulations. (g) Uncertainty of streaking direction rms in each $|\boldsymbol{k}|$ bin.

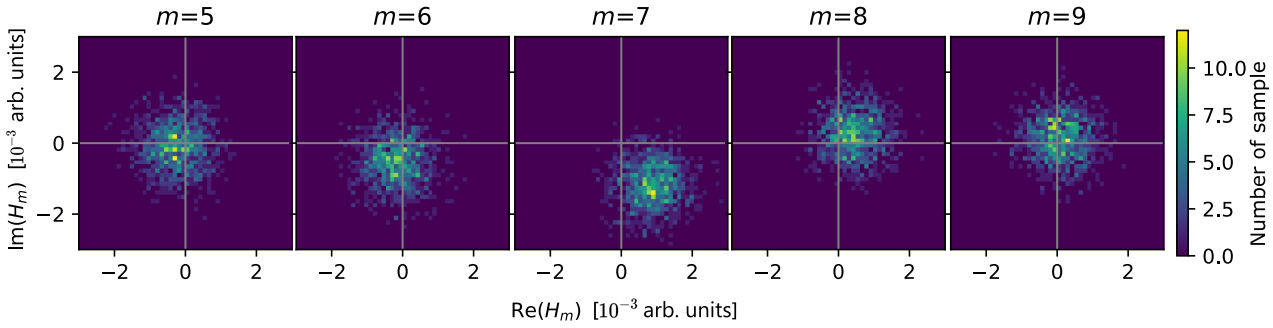

FIG. 8. Fourier coefficients' bootstrap distribution in the complex plane. The arb. unit is the same as in Fig. 4(a).

average instantaneous IR intensity of 0.7 TW/cm^2. The dipole shape of the C1s feature lessens the sensitivity to δp_y compared to δp_x, giving rise to the anisotropic distribution of the excluded shots. We estimated the uncertainty of streaking direction σ_κ by projecting the uncertainty ellipsoid to the angular dimension:

$$\sigma_\kappa = \{\mathrm{Var}[\mathrm{atan2}(q_y, q_x)]\}^{1/2}, \qquad \boldsymbol{q} \sim \mathcal{N}(\boldsymbol{k}, \Sigma), \quad \text{(B1)}$$

where $\boldsymbol{q}$ is a normally distributed random vector, centered at $\boldsymbol{k}$, and atan2 is the four-quadrant inverse tangent function. The covariance of the normal distribution is $\Sigma = (s^2\epsilon/2\ln\alpha)H^{-1}$, with $1-\alpha = 0.95$ ensuring the probability enclosed in the uncertainty ellipsoid equals the probability of correctly identifying a mistimed shot. A validation of this uncertainty estimation method is presented in Supplemental Material Fig. S5 [34]. As shown in Fig. 7(g), the uncertainty σ_κ correlated with the streaking shift amplitude, yielding an average of $\overline{\sigma}_\kappa = 0.24$ rad root mean square. For each κ frame, we normalized and offset the average image of the cotimed shots, such that in two detector regions the yield agreed with the average mistimed image: the C1s feature and the detector edge ($5.43 < p_r < 5.74$ a.u., no sample-related electron count).

2. Estimation of errors

The standard error of the mean presented in Figs. 3 and 4 was calculated with 1000 bootstrap samples [48] of the main dataset consisting of $N_c = 4\times10^4$ cotimed shots and $N_m = 2\times10^4$ mistimed shots. The bootstrap distribution of coefficient H_m is approximately normal, as shown in Fig. 8. In the Hotelling's t^2-tests [40] on H_m, our null hypothesis is that the underlying complex-valued Fourier coefficient is zero. Using the bootstrap samples, for H_7 we evaluated the t^2 statistic to be 6.124, corresponding to a p value less than 0.05, revealing significance and rejecting the null hypothesis. In addition to the bootstrap variance, the reported uncertainty of the retrieved lifetime had incorporated the effect of finite detector momentum resolution $\sigma_p = 0.014$ a.u. on the ROI boundary uncertainty.

3. Measurement of noise level

The noise level shown in Figs. 4(a) and 4(e) is measured *in situ* by comparing two subsets of the mistimed shots in the same set of $N_\theta = 36$ angular bins as for the AM signal. Splitting the two subsets according to the $N_c/N_m \approx 2$ ratio, we treated the larger subset as if the shots were cotimed to obtain the DMD referenced to the average of the smaller subset. Then we integrated the differential yield in the angular bins and conducted the delay-invariant averaging, in the same way as for $\overline{Y_{\mathrm{AM}}}(\phi)$. Since both subsets contain only mistimed shots, the expectation of the differential yield is zero, and the measured difference characterizes the noise level. We randomized the split 10 times, drawing 100 bootstrap samples for each split. The bootstrap variance of the noise was scaled by $N_m/(N_m+N_c)$ according to the central limit theorem in order to be comparable with the main dataset.

4. Comparison with photoelectron features

Similar to the differential AM yield $Y_{\mathrm{AM}}(\theta,\kappa)$, we also measured the differential yield of the C1s photoelectrons $Y_C(\theta,\kappa)$ and of the valence photoelectrons $Y_{\mathrm{V}}(\theta,\kappa)$, in their respective ROIs. Performing the delay-invariant averaging, we obtain $\overline{Y_C}(\phi)$ and $\overline{Y_{\mathrm{V}}}(\phi)$, respectively, and their Fourier amplitudes are presented in Fig. 9(a). The Fourier coefficients of $\overline{Y_C}$ and $\overline{Y_{\mathrm{V}}}$ are also located at integers of m, and the horizontal offset in Fig. 9(a) is for visual clarity. In contrast to the AM signal, around $m = 7$ neither the C1s feature or the valence feature exhibits a peak in Fig. 9(a). Rather, their Fourier amplitudes decreases with increasing m and converge to their respective *in situ* noise levels, which is consistent with their property of emitting in a timescale much shorter than the IR period. A minor difference from the AM feature is the dipole shape of the photoelectrons' momentum distributions. Thus in the delay-invariant averaging of the photoelectrons, we limited to the 26 angular bins within ±1.0 and $\pi\pm1.0$ rad, as shown in Fig. 9(b), but still, all 40 frames are involved, keeping the resultant $\overline{Y_C}(\phi)$ and $\overline{Y_{\mathrm{V}}}(\phi)$ uniformly sampled across the period. The lack of structure in the measured C1s

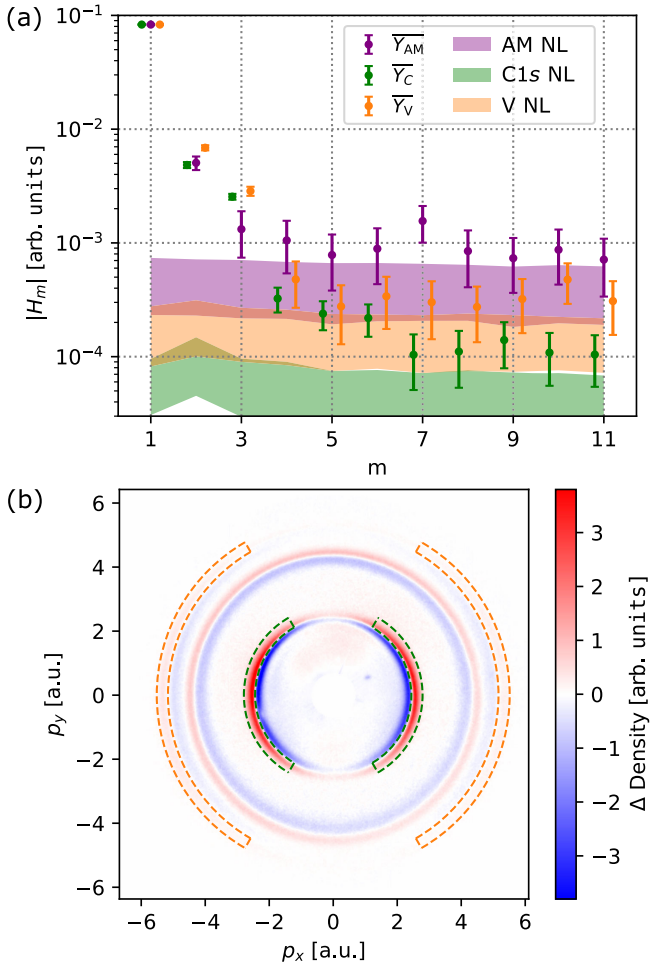

FIG. 9. Comparison with the C1s feature and valence feature. (a) Fourier coefficient amplitudes of the measured signals in three different features: AM [purple dots; same as Fig. 4(a)], C1s (green dots), and valence (orange dots). The C1s and the valence signals are normalized to the AM signal in $|H_1|$. Error bars represent $\pm\sigma_{\bar{x}}$. The shades in corresponding colors represent the mean $\pm\sigma_{\bar{x}}$ range of the noise level (NL) characterized for each feature *in situ*; see Sec. B 3. (b) DMD averaged over streaking shift directions κ. Dotted boxes mark the ROIs for the C1s (green) and valence (orange) photoelectron features.

and valence signals indicates that the $|H_7|$ peak in the AM signal is a behavior present only in the AM emission.

5. Model of valence feature

Since the valence photoelectrons are well separated from the AM electrons in KE, they contribute to the ROI only due to the projection in c-VMI. Here, we describe how the contribution from the valence photoelectrons to the DMD is reconstructed from the measurement. We first reconstructed the dressing-free momentum spectrum $W^{(0)}(\boldsymbol{p})$ from the measurement of its corresponding z projection $V^{(0)}(\theta, p_r)$. Since the valence photoelectrons result from direct ionization, the momentum spectrum consists of

$$W^{(0)}(\boldsymbol{p}) = \sigma_0(p)[1 + \beta_2(p)P_2(p_x/p)], \tag{B2}$$

where $\sigma_0(p)$ is the cross section, $\beta_2(p)$ is the anisotropy parameter, and P_2 is the second-order Legendre polynomial [49]. The corresponding KE spectrum is proportional to $\sqrt{E}\sigma_0(\sqrt{2mE})$. The total KE spectrum measured in the IR–x-ray mistimed case has been shown in Fig. 1(d), with $\beta_2(p) \simeq 2$ across the valence feature, but the reconstruction of valence is affected by the intense AM feature nearby, as shown in the magnified view in Fig. 10(a). Tuning the x-ray central photon energy to 276 eV, below the lowest carbon core-excited resonance at 285.0 eV [39], we measured the valence KE spectrum without AM, and the result reasonably agrees with the ∼374 eV x-ray (above threshold) spectrum after a KE shift. We therefore replaced the low-energy part (KE < 328 eV) of the KE spectrum with the KE-shifted below-resonance results and extrapolated $\beta_2 = 2$ to reconstruct $W^{(0)}(\boldsymbol{p})$ according to Eq. (B2). The reconstruction of momentum spectra was conducted with the pBasex algorithm [50], using a set of Gaussian radial basis $f_h(p) = \exp[-(p - p_h)^2/(2\sigma_{pb}^2)]$ with $\sigma_{pb} = 0.009$ a.u. and the centers spaced by a c-VMI pixel $p_{h+1} - p_h = 0.0125$ a.u. In all the reconstructions, we have accounted for a collection efficiency map that depends only on the angle between momentum and z axis. This map was characterized with the measured C1s feature and x-ray spectra $I(\omega)$, and its nonuniformity is attributed to the longitudinal spread of the ionized gas target, according to simulations of our c-VMI design. The measured valence feature in the KE spectrum is consistent with the binding energy, as shown in Fig. 10(a). The deepest valence binding energy is calculated at the RHF level and the others are measured [35,36].

Next, we reconstructed the IR-dressed valence feature based on the measured DMD in the $p_r > 5.0$ a.u. region, where the KE (>340 eV) is unambiguously high such that no AM electron can be imaged in that region. Since the valence ionization is nearly instantaneous, the streaking effect is modeled as a momentum shift, yet the momentum shift directions of the valence photoelectrons weakly depend on KE due to the photoemission delay. Reconstructed with pBasex, $W^{(0)}(\boldsymbol{p})$ naturally decomposes into the components on the radial basis $W^{(0)}(\boldsymbol{p}) = \sum_h W_h^{(0)}(\boldsymbol{p})$, and each component $W_h^{(0)}(\boldsymbol{p})$ is an energy shell centered at the KE value of $p_h^2/(2m)$. The z projection of two example KE shells $V_h^{(0)}$ is shown in Fig. 10(b). In this way, we model the IR-dressed momentum spectrum $W^{(s)}(\boldsymbol{p})$ as

$$W^{(s)}(\boldsymbol{p};\boldsymbol{k}) = \sum_h W_h^{(0)}(\boldsymbol{p} - \hat{R}_z(\delta_h)\boldsymbol{k}), \tag{B3}$$

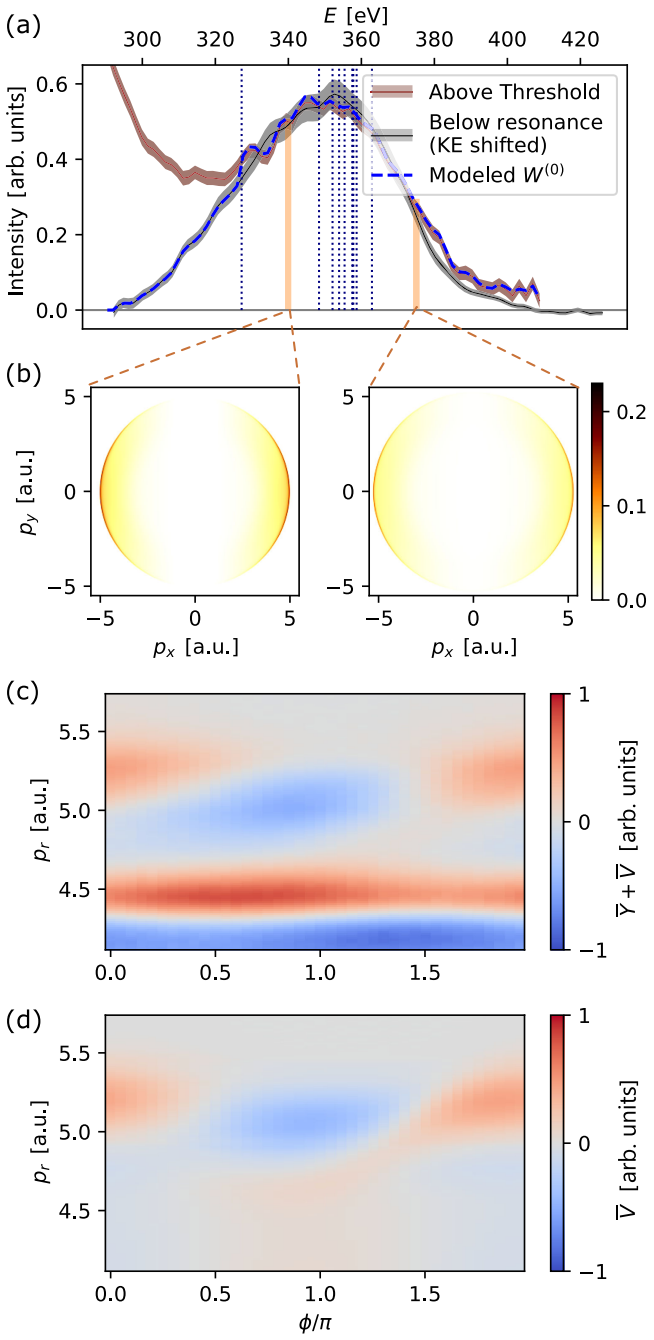

FIG. 10. Model for the valence feature. (a) Reconstruction of $V^{(0)}$ from the measured IR-mistimed distribution. The above-threshold spectrum (brown) is from Fig. 1(d). The below-resonance spectrum (black) has been shifted in KE and normalized to match with the above-threshold counterpart. Shaded areas cover $\pm 2\sigma_{\bar{x}}$. KE spectrum of $V^{(0)}$ is shown in dashed line. Dotted lines mark the KE corresponding to the valence binding energy of valence orbitals given photon energy 374 eV. (b) Projection of $V^{(0)}$ along the c-VMI axis for two example slices of KE, as indicated by the orange shades in (a). (c),(d) Delay-invariant average over θ of the (c) measured DMD of all electrons and the (d) reconstructed DMD of valence photoelectrons.

where the momentum shift of the KE shell $W_h^{(0)}$ is modeled as a result of rotating the C1s momentum shift $\boldsymbol{k} = e\boldsymbol{A}(t_i)$ by angle δ_h about the z axis. Because of the linearity of the projection, Eq. (B3) also describes the relation between $V^{(s)}(\theta, p_r; \boldsymbol{k})$ and $V_h^{(0)}(\theta, p_r)$, i.e., the projections of $W^{(s)}$ and $W_h^{(0)}$, respectively. We further parametrized the rotation angles as $\delta_h = \beta[p_h^2/(2m) - E_c]$ with parameters E_c and β. Then the DMD of valence photoelectrons $V(\theta, p_r, \kappa)$ is modeled as $V^{(s)} - V^{(0)}$ averaged over the experimental distribution of $|\boldsymbol{k}|$ [see Fig. 7(f)]. Fitting the model to the measured DMD in the $p_r > 5.0$ a.u. region, we obtain the optimal point at $E_c = 355.5$ eV and $\beta = 0.0122$ rad/eV. The delay-invariant average of the best-fit valence photoelectron DMD is denoted as $\bar{V}(\phi, p_r) = \sum_{q=1}^{N_\theta} V(\theta_q, p_r; \kappa = \theta_q - \phi)/N_\theta$, following the notation convention in the main text. The delay-invariant average of the experimentally measured total DMD is shown in Fig. 10(c). This consists of the contribution from the AM electrons $\bar{Y}(\theta, p_r)$ and the contribution from the valence photoelectrons $\bar{V}(\theta, p_r)$, the latter of which is shown in Fig. 10(d), where we see the model well reproduces the measured DMD in the $p_r > 5.0$ a.u. region. Therefore we subtracted the modeled valence DMD from the total DMD, across the region where the AM feature or the valence feature are present. The p_r bins in Figs. 10(c) and 10(d) are one c-VMI pixel (0.0125 a.u. momentum) wide, the same as Fig. 2(f). The polar rebinning was performed using the PYFAI package [51].

APPENDIX C: QUANTUM-MECHANICAL MODEL

In Eq. (3), we have assumed the population loss of C1s^{-1} states to be exponential, with a single rate Γ as the average inverse lifetime $\Gamma = (\Gamma_H + \Gamma_F)/2$, because we have found the simulated AM distribution insensitive to $\Gamma_H - \Gamma_F$ within 20% relative difference. In all three simulation results shown in Fig. 4, the average core-vacancy lifetime is the measured 6.5 fs. The two AM transition matrix elements M_α are assumed to be the same and uniform in the momentum region of interest.

The x-ray pulse is modeled as a Gaussian pulse with 5.6 eV FWHM bandwidth, and the IR is modeled as a Gaussian pulse with 71 fs FWHM duration. Both pulses in the calculations are Fourier transform limited, and the phase of the carrier is set to zero. Because the dressing-free AM distribution is isotropic in this model, varying κ (the IR phase at the x-ray arrival time) is equivalent to a z rotation of the AM distribution $\rho_A(\theta, p_r, p_z; \kappa) = \rho_A(\theta - \kappa, p_r, p_z; 0)$, where we adopt cylindrical coordinates of the AM momentum. Therefore, the delay-invariant averaging keeps the modeled distribution ρ_A unchanged, resulting in $\rho_A(\phi, p_r, p_z; 0)$. In all the simulations, we have

accounted for the c-VMI projection by integrating $\rho_A(\boldsymbol{p})$ along p_z and then applied a two-dimensional Gaussian filter according to the detector momentum resolution ($\sigma_p = 0.014$ a.u.). We have also averaged over the amplitude of streaking shift $|e\boldsymbol{A}(t_i)|$ by weighting simulations at 14 different amplitudes according to the measured distribution. The weight of each single-amplitude simulation equals to the area between the vertical gray lines in the histogram shown in Fig. 7(f). For each single-amplitude simulation, an additional Gaussian filter along the angular dimension was applied according to the measured root mean square of σ_κ at this amplitude, Fig. 7(g).

For the coherent model, the cationic energies I_α are set to the experimental values [21,22]. The single final dicationic energy is set to $I^{(2)} = 35.5$ eV such that the peak-lobes signature in $|H_7(p_r)|$ shown in Fig. 4(c) aligns with the measurement in p_r. In the coherent model, the normalized coherence of the R-IDM is $|R_{\mathrm{HF}}|/\sqrt{R_{\mathrm{HH}}R_{\mathrm{FF}}} = 0.61$, assuming the photoelectron angular distributions associated with the carbon sites are the same. Since the ratio of the measured $|H_7|$ to the coherent model is 0.71, when simulating the hole 1-RDM $\Delta\rho$ in Fig. 5, we initiated the normalized coherence of the R-IDM as 0.43, according to the ratio in $|H_7|$.

We briefly return to the equivalence between the effective delay $\tau_\phi = \phi/\omega_L$ and the AM delay τ. The approximation $\tau_\phi \approx \tau$ is valid at what we have called the high-momentum edge, which can help interpret the streaking signal in the time domain [14]. The comparison between the SFA calculations and the measurement, however, is still valid outside this region. We choose the experimental ROI to be lower than the high-momentum edge, in order to capture significant amplitude from the lower-energy AM channels associated with the C_H core vacancy. On the other hand, to maintain the dominance of the pathways with outward AM streaking directions, we set the radial lower bound of the ROI at the maximal point of the radial gradient of the IR-mistimed AM distribution. In our ROI, as illustrated in Fig. 3(a), each effective delay τ_ϕ corresponds to a range of AM delay τ. However, the effective delay still corresponds to the same range of τ across different angular positions, which allows the delay-invariant averaging. This momentum-delay convolution plays a role in the encoding of the time-dependent emission rate into the observable. When the streaking amplitude is small, this convolution suppresses the high-frequency components relative the low frequencies, which explains the emphasis on the $m = 1$ Fourier component observed in Fig. 3(b). This trend in frequency response can be mitigated by increasing the streaking amplitude. A comparison between time-dependent emission rate and the observable is presented in Supplemental Material Fig. S2 [34].

1. Mapping from ionic coherence

The complex amplitude in Eq. (3) also demonstrates the mapping from the ionic coherence R_{HF} to the interference in the total AM distribution $\rho_A(\boldsymbol{p}_a)$:

$$\int d^3\boldsymbol{p}_p b_{\mathrm{F}}^* b_{\mathrm{H}} = M_{\mathrm{H}} M_{\mathrm{F}}^* \int_{t_b}^{\infty} dt_1 \int_{t_b}^{\infty} dt_2 \tilde{R}_{\mathrm{HF}}(t_1, t_2) \times e^{iI^{(2)}(t_1 - t_2) + iS(t_1, t_2, \boldsymbol{p}_a)}, \tag{C1}$$

Here $\tilde{R}_{\mathrm{HF}}(t_1, t_2) = \int d^3\boldsymbol{p} \langle \Phi_{\mathrm{H}}^+, \boldsymbol{p} | \Phi(t_1) \rangle \langle \Phi(t_2) | \boldsymbol{p}, \Phi_{\mathrm{F}}^+ \rangle$, $|\Phi_\alpha^+\rangle$ is the $C_\alpha 1s^{-1}$ state, and $|\Phi(t)\rangle$ is the N-electron wave function after absorbing one x-ray photon. The derivation of Eq. (C1) is in Sec. I. 2 of Supplemental Material [34]. The simultaneous part of the time correlation $\tilde{R}_{\mathrm{HF}}(t, t) = R_{\mathrm{HF}}(t)$ is identical to the coherence in the R-IDM. Note that the t_1 and t_2 in Eq. (C1) are the AM emission times illustrated in Fig. 3(a), so they are both around θ/ω_L for a general $\boldsymbol{p}_a$ located on the higher-energy side of the IR-mistimed spectrum. As κ is scanned, we scan the effective delay $\tau_\phi = (\theta - \kappa)/\omega_L$, but there is also blurring by the temporal correlations in the vicinity of the simultaneous ($t_1 = t_2$) line.

2. Geometry averaging

For the geometry averaging, we generated the geometries in the dimensionless normal coordinates Q_v by sampling from the probability distribution $\propto \exp(-\sum_{v=0}^{N_V-1} Q_v^2)$ of the vibrational ground state of the g.s. molecule. The $N_V = 12$ normal modes are calculated at the level of RHF aug-cc-pwCVTZ, using the GAMESS package [52]. Based on these normal modes, we converted the normal coordinates Q_v to the Cartesian-coordinate displacements of atomic sites. For each of the 1000 geometries, we first calculated energy $E_{\mathrm{g.s.}}$ of the molecule, at the level of configuration interaction using the molecular orbitals (MOs) from RHF 6-31G(d,p). Then the energy $E[C_\alpha 1s^{-1}]$ is calculated as the lowest eigenenergy in the restricted space where the configurations of the bound $N-1$ electron system contain a single core vacancy at the C_α site. The transition energy is $I_\alpha = E[C_\alpha 1s^{-1}] - E_{\mathrm{g.s.}}$. To converge the configuration interaction efficiently, we adopted the MOs of the $NH_2CF_2^{2+}, CH_2NF_2^{2+}$ ions, for $\alpha = \mathrm{H}, \mathrm{F}$, respectively. These auxiliary MOs are calculated at the level of restricted open-shell Hartree-Fock 6-31G(d,p) at the equilibrium geometry of the CH_2CF_2 molecule. Next, we calculated the dicationic ground state energy E_{2+} using the MO of CH_2CF_2, obtaining $I^{(2)} = E_{2+} - E_{\mathrm{g.s.}}$. At this level of theory, we believe the relative differences of these transition energies, among the geometries in the vicinity of the equilibrium, are acceptably accurate. Thus for each transition energy (I_{H}, I_{F}, or $I^{(2)}$), the geometry sample is collectively shifted to match the equilibrium values with the respective values

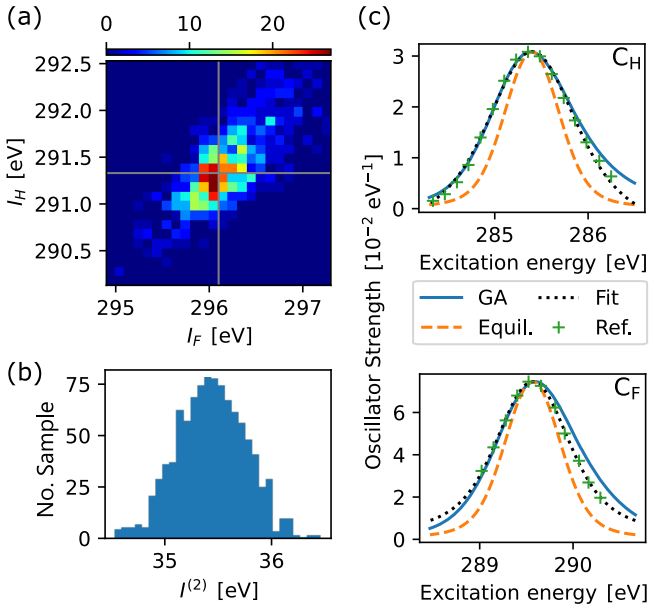

FIG. 11. Distribution of the geometry sample for GA. (a),(b) Histograms of the transition energies used in the GA model, for the 1000 molecular geometries sampled from the vibrational g.s. Panel (a) shows (I_H, I_F). Panel (b) shows $I^{(2)}$. (c) Comparison on the linewidths calculated with (blue solid line) and without (orange dashed line) GA, to the measurement results of the C1$s \to \pi^*$ absorption features (green cross; measured by McLaren *et al.* [39]). The upper and lower panels are on the C_H and C_F sites, respectively. The measured data points are fitted with a Voigt profile (black dotted line), where the optimal Lorentzian parameters are $\gamma_H = 1/(1.5\ \text{fs})$ and $\gamma_F = 1/(2.3\ \text{fs})$, respectively, with $\sigma_E = 0.25$ eV fixed.

used in the fully coherent SFA model. The distribution of the geometry sample is visualized in Figs. 11(a) and 11(b).

As a validation of the sampled energy spread, we assumed the core-vacancy lifetime and geometry dependence of the C1$s \to \pi^*$ core-excited molecular states are the same as the corresponding cation. The calculated linewidths of the C1$s \to \pi^*$ absorption features, with and without the GA, are compared to the experimental results [39], as shown in Fig. 11(c). A $\sigma_E = 0.25$ eV Gaussian blurring has been included in the calculations according to the reported resolution in Ref. [39]. With only the equilibrium geometry, the linewidths from the *ab initio* calculations $[\Gamma_H = 1/(6.1\ \text{fs}),\ \Gamma_F = 1/(6.9\ \text{fs})$; see Appendix D] are notably narrower than the absorption features measured with spectroscopy. With the GA, the calculated linewidths better agree with the measurement, especially on the $C_H 1s \to \pi^*$ feature. This corroborates the spread of I_α in the geometry sample. To obtain a lower bound of the core-vacancy lifetime, we fitted a Voigt function to each measured line shape, obtaining an average Lorentzian width of $1/(1.8\ \text{fs})$, as shown Fig. 11(c).

APPENDIX D: *AB INITIO* CALCULATIONS OF LIFETIME

We have employed the Fano algebraic diagrammatic construction (ADC) method [53] to compute *ab initio* the lifetimes of the two core-ionized states in CH_2CF_2. Converged results were obtained with the aug-cc-pwCVQZ one-particle basis set. The classification of the ADC configuration space into the boundlike ($\mathcal{Q}$) and continuumlike ($\mathcal{P}$) subspaces was implemented using the *scheme B* [53] with 144 energetically accessible final dicationic states defining the $\mathcal{P}$ subspace. Unfortunately, the molecule is too large to apply the consistent ADC(2,2) scheme. Therefore, we were limited to the Fano-ADC(2)x method, which systematically underestimates the decay widths due to inconsistency in the representation of the initial and final states of the decay process.

The calculated K-shell binding energies are 290.73 and 295.82 eV for the C_H and C_F sites, respectively. The resulting difference $\Delta I_C^{(th)} = 5.08$ eV is in reasonable agreement with the observed $\Delta I_C = 4.77$ eV. Using Fano-ADC(2)x, we obtained the respective decay widths 87 and 77 meV for the two core-ionized states. The corresponding average lifetime 8.1 fs exceeds the observed lifetime 6.5 ± 0.8 fs, which we attribute to the inconsistency of the Fano-ADC(2)x method mentioned above.

To obtain a more accurate theoretical estimate of the lifetimes, we have performed a series of Fano-ADC(2)x and Fano-ADC$(2,2)_m$ calculations for methane and its fluorinated derivatives, together with ethane, ethene, and ethyne to include both the effects of fluorination and double or triple bond between the carbons. The results, obtained using the same one-particle basis set, are collected in Table I. Importantly, the ratio $\Gamma_{(2,2)}/\Gamma_{(2)x} = 1.24 \pm 0.02$ is almost independent of the molecule. This observation allows us to extrapolate the decay widths of 1,1-difluoroethene core-ionized states as 108.0 ± 2.1 meV for the CH_2 site and 95.5 ± 1.9 meV for the CF_2 site, respectively. This extrapolation thus results in an averaged lifetime of 6.5 ± 0.1 fs consistent with the experiment.

TABLE I. Carbon core-hole decay widths calculated by Fano-ADC(2)x and Fano-ADC$(2,2)_m$ schemes. The last column shows the ratio $\Gamma_{(2,2)}/\Gamma_{(2)x}$.

	Γ (meV)		
	ADC(2)x	ADC$(2,2)_m$	Ratio
CH_4	89.6	108.9	1.21
CH_3F	83.1	103.8	1.25
CH_2F_2	77.9	97.9	1.26
C_2H_6	85.5	105.9	1.24
C_2H_4	85.0	106.2	1.25
C_2H_2	88.5	110.3	1.25

APPENDIX E: SEMICLASSICAL MOLECULAR GEOMETRY EVOLUTION

Difference in potential energy surfaces (PESs) can lead to different motions of the molecular geometry. The effect of diverging vibrational wave packets on the electronic coherence has been discussed and experimentally explored [42,43]. We follow the semiclassical approach detailed in Ref. [42] to simulate the evolution of the overlap χ between the two vibrational wave packets of the $C_\alpha 1s^{-1}$ states. This simulation assumes the vibrational wave packets maintain the same Gaussian shape as the ground state,

$$\chi(t) = e^{-d(t)^2/4} e^{iS_A(t)}, \tag{E1}$$

where $d(t)$ is the phase-space (Q, P) distance between the two classical trajectories, $S_A(t)$ is the classical action, and P_v is the dimensionless momentum conjugate to the dimensionless normal coordinate Q_v. The classical vibrational Hamiltonian is $H_{\text{vib}} = (\hbar/2)\sum_{v=0}^{11} P_v \omega_v P_v + W(Q)$, with ω_v denoting the angular frequency of the normal mode v and $W(Q)$ denoting the potential energy surface. For each core-vacancy cationic state $C_\alpha 1s^{-1}$, we integrate the equation of motion according to the corresponding vibrational Hamiltonian to obtain a classical trajectory $(Q^{(\alpha)}(t), P^{(\alpha)}(t))$. The resultant two trajectories are separated by $d(t) = \sqrt{\Delta Q(t)^2 + \Delta P(t)^2}$ in the phase space, where $\Delta Q = \|Q^{(\mathrm{H})} - Q^{(\mathrm{F})}\|$ and $\Delta P = \|P^{(\mathrm{H})} - P^{(\mathrm{F})}\|$ are the coordinate and momentum distances, respectively.

The symmetry of the $C_\alpha 1s^{-1}$ states simplifies the classical trajectory simulation. Since both carbon K-shell orbitals belong to the A_1 irreducible representation ("irrep") of the molecule's symmetry group C_{2v}, the corresponding PESs also belong to the A_1 irrep. As a result, the motion of the molecular geometry is active only along the five A_1-irrep normal modes, while classically remaining at $Q_v = 0$, $P_v = 0$ along the other seven normal modes. We sampled ~800 molecular geometries in the A_1-irrep subspace from a uniform distribution $Q_v \sim \mathcal{U}_{\text{niform}}[-5, 5]$, while keeping the non-$A_1$ modes frozen at $Q_v = 0$, to calculate the two cationic PESs $W_\alpha(Q)$ by a fourth-order polynomial fit in the five-dimensional space. Three slices of the PESs are visualized in Fig. 12(a). As shown in Fig. 12(b), both ΔQ and ΔP increase within the first 10 fs, which diminishes the magnitude of the overlap $|\chi|$. Moreover, the phase of the electronic coherence is affected by the diverging trajectories in molecular geometry evolution. The classical action $S_A(t) = -\Delta I_C t + S_{\text{red}}(t)$ consists of the dynamical phase accumulated according to the total energy difference ΔI_C and the reduced action [42]:

$$S_{\text{red}}(t) = \int_0^t dt' \sum_v (P_v^{(F)}(t')\dot{Q}_v^{(F)}(t') - P_v^{(H)}(t')\dot{Q}_v^{(H)}(t')), \tag{E2}$$

which is shown in Fig. 12(c). This indicates that the molecular geometry evolution constitutes a dephasing mechanism with effects in both amplitude and phase of the coherence. The magnitude of the overlap $|\chi|$ drops to $1/e$ at $t = 4$ fs according to the calculated classical trajectories. As pointed out in Sec. IV, ignoring the dispersion of vibrational wave packets underestimates the dephasing time. Therefore, the actual dephasing time from vibrational motions could be comparable to or longer than the 6.5 ± 0.8 fs core-vacancy lifetime.

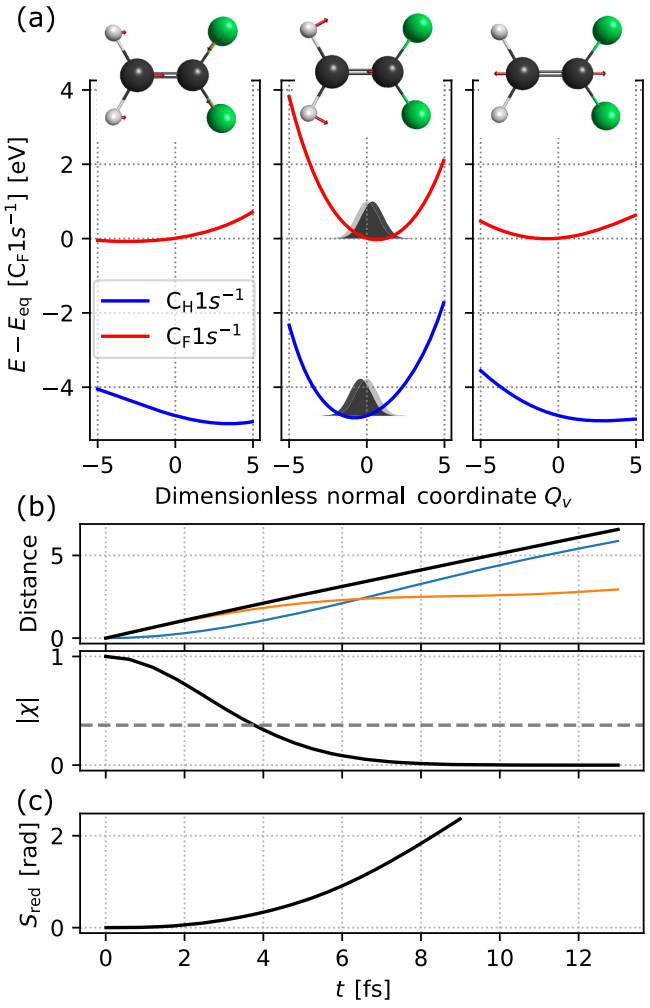

FIG. 12. Semiclassical molecular geometry evolution of the two $C_\alpha 1s^{-1}$ cationic states. (a) Slices of potential energy surfaces associated with the $C_H 1s^{-1}$ (blue lines) and $C_F 1s^{-1}$ (red lines) states. Energy is referenced to the energy of $C_F 1s^{-1}$ at the molecular equilibrium geometry. Each normal mode is visualized in the illustration. For the $v = 8$ mode, we present the probability density of the wave packets with shadings, at $t = 0$ (light gray) and $t = 4$ fs (dark gray). (b) Upper: time evolution of the distance between the two classical trajectories: in coordinate ΔQ (blue line), in momentum ΔP (orange line), and in phase space d (black line). Lower: overlap between the wave packets. Dashed line marks $1/e$. (c) Reduced action calculated with the classical trajectories.

[1] J. Duris, S. Li, T. Driver, E. G. Champenois, J. P. MacArthur, A. A. Lutman, Z. Zhang, P. Rosenberger, J. W. Aldrich, R. Coffee, G. Coslovich *et al.*, *Tunable isolated attosecond x-ray pulses with gigawatt peak power from a free-electron laser*, Nat. Photonics **14**, 30 (2020).

[2] M. Kretschmar, E. Svirplys, M. Volkov, T. Witting, T. Nagy, M. J. J. Vrakking, and B. Schütte, *Compact realization of all-attosecond pump-probe spectroscopy*, Sci. Adv. **10**, eadk9605 (2024).

[3] Z. Guo, T. Driver, S. Beauvarlet, D. Cesar, J. Duris, P. L. Franz, O. Alexander, D. Bohler, C. Bostedt, V. Averbukh *et al.*, *Experimental demonstration of attosecond pump–probe spectroscopy with an x-ray free-electron laser*, Nat. Photonics **18**, 691 (2024).

[4] S. Li, L. Lu, S. Bhattacharyya, C. Pearce, K. Li, E. T. Nienhuis, G. Doumy, R. D. Schaller, S. Moeller, M.-F. Lin *et al.*, *Attosecond-pump attosecond-probe x-ray spectroscopy of liquid water*, Science **383**, 1118 (2024).

[5] *The Nobel Committee for Physics, Scientific background to the Nobel Prize in Physics 2023* (2023), https://www.nobelprize.org/prizes/physics/2023/advanced-information/.

[6] G. D. Scholes, G. R. Fleming, L. X. Chen, A. Aspuru-Guzik, A. Buchleitner, D. F. Coker, G. S. Engel, R. van Grondelle, A. Ishizaki, D. M. Jonas, J. S. Lundeen, J. K. McCusker, S. Mukamel, J. P. Ogilvie, A. Olaya-Castro, M. A. Ratner, F. C. Spano, K. B. Whaley, and X. Zhu, *Using coherence to enhance function in chemical and biophysical systems*, Nature (London) **543**, 647 (2017).

[7] F. Lépine, M. Y. Ivanov, and M. J. J. Vrakking, *Attosecond molecular dynamics: Fact or fiction?*, Nat. Photonics **8**, 195 (2014).

[8] L. S. Cederbaum, W. Domcke, J. Schirmer, and W. V. Niessen, *Correlation effects in the ionization of molecules: Breakdown of the molecular orbital picture*, in *Advances in Chemical Physics* (John Wiley & Sons, Ltd, New York, 1986), pp. 115–159.

[9] A. I. Kuleff, S. Lünnemann, and L. S. Cederbaum, *Ultrafast charge migration following valence ionization of 4-methylphenol: Jumping over the aromatic ring*, J. Phys. Chem. A **114**, 8676 (2010).

[10] F. Calegari, D. Ayuso, A. Trabattoni, L. Belshaw, S. D. Camillis, S. Anumula, F. Frassetto, L. Poletto, A. Palacios, P. Decleva, J. B. Greenwood, F. Martín, and M. Nisoli, *Ultrafast electron dynamics in phenylalanine initiated by attosecond pulses*, Science **346**, 336 (2014).

[11] T. Barillot, O. Alexander, B. Cooper, T. Driver, D. Garratt, S. Li, A. Al Haddad, A. Sanchez-Gonzalez, M. Agåker, C. Arrell *et al.*, *Correlation-driven transient hole dynamics resolved in space and time in the isopropanol molecule*, Phys. Rev. X **11**, 031048 (2021).

[12] D. Schwickert, M. Ruberti, P. Kolorenč, A. Przystawik, S. Skruszewicz, M. Sumfleth, M. Braune, L. Bocklage, L. Carretero, M. K. Czwalinna *et al.*, *Charge-induced chemical dynamics in glycine probed with time-resolved Auger electron spectroscopy*, Struct. Dyn. **9**, 064301 (2022).

[13] E. P. Månsson, S. Latini, F. Covito, V. Wanie, M. Galli, E. Perfetto, G. Stefanucci, H. Hübener, U. De Giovannini, M. C. Castrovilli, A. Trabattoni, F. Frassetto, L. Poletto, J. B. Greenwood, F. Légaré, M. Nisoli, A. Rubio, and F. Calegari, *Real-time observation of a correlation-driven sub 3 fs charge migration in ionised adenine*, Commun. Chem. **4**, 73 (2021).

[14] S. Li, T. Driver, P. Rosenberger, E. G. Champenois, J. Duris, A. Al-Haddad, V. Averbukh, J. C. T. Barnard, N. Berrah, C. Bostedt *et al.*, *Attosecond coherent electron motion in Auger-Meitner decay*, Science **375**, 285 (2022).

[15] A. I. Kuleff, N. V. Kryzhevoi, M. Pernpointner, and L. S. Cederbaum, *Core ionization initiates subfemtosecond charge migration in the valence shell of molecules*, Phys. Rev. Lett. **117**, 093002 (2016).

[16] M. Ruberti, S. Patchkovskii, and V. Averbukh, *Quantum coherence in molecular photoionization*, Phys. Chem. Chem. Phys. **24**, 19673 (2022).

[17] H. Laurell, D. Finkelstein-Shapiro, C. Dittel, C. Guo, R. Demjaha, M. Ammitzböll, R. Weissenbilder, L. Neoričić, S. Luo, M. Gisselbrecht, C. L. Arnold, A. Buchleitner, T. Pullerits, A. L'Huillier, and D. Busto, *Continuous-variable quantum state tomography of photoelectrons*, Phys. Rev. Res. **4**, 033220 (2022).

[18] E. Rodríguez-Cuenca, A. Picón, S. Oberli, A. I. Kuleff, and O. Vendrell, *Core-hole coherent spectroscopy in molecules*, Phys. Rev. Lett. **132**, 263202 (2024).

[19] M. S. Schöffler, J. Titze, N. Petridis, T. Jahnke, K. Cole, L. P. H. Schmidt, A. Czasch, D. Akoury, O. Jagutzki, J. B. Williams *et al.*, *Ultrafast probing of core hole localization in* N_2, Science **320**, 920 (2008).

[20] L. Inhester, L. Greenman, A. Rudenko, D. Rolles, and R. Santra, *Detecting coherent core-hole wave-packet dynamics in* N_2 *by time- and angle-resolved inner-shell photoelectron spectroscopy*, J. Chem. Phys. **151**, 054107 (2019).

[21] W. Jolly, K. Bomben, and C. Eyermann, *Core-electron binding energies for gaseous atoms and molecules*, At. Data Nucl. Data Tables **31**, 433 (1984).

[22] D. W. Davis, M. S. Banna, and D. A. Shirley, *Core-level binding-energy shifts in small molecules*, J. Chem. Phys. **60**, 237 (1974).

[23] A. K. Kazansky, I. P. Sazhina, V. L. Nosik, and N. M. Kabachnik, *Angular streaking and sideband formation in rotating terahertz and far-infrared fields*, J. Phys. B **50**, 105601 (2017).

[24] C. Bourassin-Bouchet, L. Barreau, V. Gruson, J.-F. Hergott, F. Quéré, P. Salières, and T. Ruchon, *Quantifying decoherence in attosecond metrology*, Phys. Rev. X **10**, 031048 (2020).

[25] L.-M. Koll, L. Maikowski, L. Drescher, T. Witting, and M. J. J. Vrakking, *Experimental control of quantum-mechanical entanglement in an attosecond pump-probe experiment*, Phys. Rev. Lett. **128**, 043201 (2022).

[26] S. Nandi, A. Stenquist, A. Papoulia, E. Olofsson, L. Badano, M. Bertolino, D. Busto, C. Callegari, S. Carlström, M. B. Danailov *et al.*, *Generation of entanglement using a short-wavelength seeded free-electron laser*, Sci. Adv. **10**, eado0668 (2024).

[27] J. Itatani, F. Quéré, G. L. Yudin, M. Y. Ivanov, F. Krausz, and P. B. Corkum, *Attosecond streak camera*, Phys. Rev. Lett. **88**, 173903 (2002).

[28] M. Kitzler, N. Milosevic, A. Scrinzi, F. Krausz, and T. Brabec, *Quantum theory of attosecond XUV pulse measurement by laser dressed photoionization*, Phys. Rev. Lett. **88**, 173904 (2002).

[29] A. K. Kazansky, I. P. Sazhina, and N. M. Kabachnik, *Angular streaking of Auger-electrons by THz field*, J. Phys. B **52**, 045601 (2019).

[30] K. A. Larsen, K. Borne, R. Obaid, A. Kamalov, Y. Liu, X. Cheng, J. James, T. Driver, K. Li, Y. Liu, A. Sakdinawat, C. David, T. J. A. Wolf, J. P. Cryan, P. Walter, and M.-F. Lin, *Compact single-shot soft x-ray photon spectrometer for free-electron laser diagnostics*, Opt. Express **31**, 35822 (2023).

[31] S. Li, E. G. Champenois, R. Coffee, Z. Guo, K. Hegazy, A. Kamalov, A. Natan, J. O'Neal, T. Osipov, M. Owens, D. Ray, D. Rich, P. Walter, A. Marinelli, and J. P. Cryan, *A co-axial velocity map imaging spectrometer for electrons*, AIP Adv. **8**, 115308 (2018).

[32] M. Ruberti, *Onset of ionic coherence and ultrafast charge dynamics in attosecond molecular ionisation*, Phys. Chem. Chem. Phys. **21**, 17584 (2019).

[33] J. M. Glownia, J. Cryan, J. Andreasson, A. Belkacem, N. Berrah, C. I. Blaga, C. Bostedt, J. Bozek, L. F. DiMauro, L. Fang *et al.*, *Time-resolved pump-probe experiments at the LCLS*, Opt. Express **18**, 17620 (2010).

[34] See Supplemental Material at http://link.aps.org/supplemental/10.1103/PhysRevX.15.011008 for details of theoretical modeling and supporting videos.

[35] R. Locht, D. Dehareng, and B. Leyh, *The spectroscopy of the geminal ethylene difluoride* $(1,1\text{-}C_2H_2F_2)$*: The* HeI*, threshold and constant ion state photoelectron spectroscopies*, J. Phys. B **45**, 115101 (2012).

[36] G. Bieri, L. Åsbrink, and W. V. Niessen, *30.4-nm* He(II) *photoelectron spectra of organic molecules: Part IV. Fluoro-compounds* (C, H, F), J. Electron Spectrosc. Relat. Phenom. **23**, 281 (1981).

[37] D. C. Haynes, M. Wurzer, A. Schletter, A. Al-Haddad, C. Blaga, C. Bostedt, J. Bozek, H. Bromberger, M. Bucher, A. Camper *et al.*, *Clocking Auger electrons*, Nat. Phys. **17**, 512 (2021).

[38] T. Åberg, *Unified theory of Auger electron emission*, Phys. Scr. **T41**, 71 (1992).

[39] R. McLaren, S. A. C. Clark, I. Ishii, and A. P. Hitchcock, *Absolute oscillator strengths from K-shell electron-energy-loss spectra of the fluoroethenes and 1,3-perfluorobutadiene*, Phys. Rev. A **36**, 1683 (1987).

[40] H. Hotelling, *The generalization of student's ratio*, Ann. Math. Stat. **2**, 360 (1931).

[41] M. Vacher, J. Meisner, D. Mendive-Tapia, M. J. Bearpark, and M. A. Robb, *Electronic control of initial nuclear dynamics adjacent to a conical intersection*, J. Phys. Chem. A **119**, 5165 (2015).

[42] N. V. Golubev, T. Begušić, and J. Vaníček, *On-the-fly ab initio semiclassical evaluation of electronic coherences in polyatomic molecules reveals a simple mechanism of decoherence*, Phys. Rev. Lett. **125**, 083001 (2020).

[43] D. T. Matselyukh, V. Despré, N. V. Golubev, A. I. Kuleff, and H. J. Wörner, *Decoherence and revival in attosecond charge migration driven by non-adiabatic dynamics*, Nat. Phys. **18**, 1206 (2022).

[44] O. E. Alon, A. I. Streltsov, and L. S. Cederbaum, *The multiconfigurational time-dependent Hartree method for identical particles and mixtures thereof*, in *Multidimensional Quantum Dynamics* (John Wiley & Sons, Ltd, Hoboken, 2009), Chap. 17, pp. 185–207.

[45] P. Franz, S. Li, T. Driver, R. R. Robles, D. Cesar, E. Isele, Z. Guo, J. Wang, J. P. Duris, K. Larsen *et al.*, *Terawatt-scale attosecond x-ray pulses from a cascaded superradiant free-electron laser*, Nat. Photonics **18**, 698 (2024).

[46] J. Wang, T. Driver, F. Allum, C. C. Papadopoulou, C. Passow, G. Brenner, S. Li, S. Düsterer, A. T. Noor, S. Kumar, P. H. Bucksbaum, B. Erk, R. Forbes, and J. P. Cryan, *Photon energy-resolved velocity map imaging from spectral domain ghost imaging*, New J. Phys. **25**, 033017 (2023).

[47] A. Kaehler and G. Bradski, *Learning opencv 3* (O'Reilly Media, Sebastopol, 2016), Chap. 13.

[48] B. Efron, *Bootstrap methods: Another look at the jackknife*, Ann. Stat. **7**, 1 (1979).

[49] C. N. Yang, *On the angular distribution in nuclear reactions and coincidence measurements*, Phys. Rev. **74**, 764 (1948).

[50] G. A. Garcia, L. Nahon, and I. Powis, *Two-dimensional charged particle image inversion using a polar basis function expansion*, Rev. Sci. Instrum. **75**, 4989 (2004).

[51] J. Kieffer, V. Valls, N. Blanc, and C. Hennig, *New tools for calibrating diffraction setups*, J. Synchrotron Radiat. **27**, 558 (2020).

[52] G. M. J. Barca *et al.*, *Recent developments in the general atomic and molecular electronic structure system*, J. Chem. Phys. **152**, 154102 (2020).

[53] P. Kolorenč and V. Averbukh, *Fano-ADC(2,2) method for electronic decay rates*, J. Chem. Phys. **152**, 214107 (2020).